R675

Technical Report

STRESS ANALYSIS OF A CONICAL ACRYLIC VIEWPORT

April 1970

Sponsored by

NAVAL FACILITIES ENGINEERING COMMAND

NAVAL CIVIL ENGINEERING LABORATORY

Port Hueneme, California

69

STRESS ANALYSIS OF A CONICAL ACRYLIC VIEWPORT

Technical Report R-675

YF 38.535.005.01.005

by

M. R. Snoey and J. E. Crawford

ABSTRACT

This study was initiated to: (1) determine experimentally the structural response of a viewport design, (2) determine the accuracy of the finite element method in predicting viewport behavior by comparing analytical to experimental results, and (3) determine the effect, if any, of the flange surface finish on the structural behavior of the viewport using both experimental and analytical techniques. In the experimental phase, four, full-scale, conical acrylic viewports, with a nominal thickness-to-minor-diameter ratio of 0.5 and an included angle of 90^{o}, were strain-gaged and tested to 8,000 psi. In the analytical phase, the same viewport design was analyzed with a finite element computer program. The finite element results successfully bracketed the experimental results by assuming two extreme boundary conditions, fixed and free, at the viewport-flange interface. The fixed condition assumed an infinite coefficient of friction, and the free condition assumed zero friction. In addition, the finite element analysis provided complete internal stress distributions. All results indicated that viewports with this design exhibit both plugging and bending behavior and have two areas of high stress concentration, the center of the high-pressure face and the corner between the low-pressure face and the conical bearing surface. The analytical investigation indicated that the surface finish of the flange significantly affects the viewport stress distribution. A rough flange surface (fixed case) produces stress magnitudes in the viewport which are about 25% less than those in the viewport with a smooth flange surface (free case). This was also established experimentally by tests of 15 model viewports under equal load, which indicated that a 125 rms flange finish caused less plastic deformation in the viewports than either a 63 or 32 rms flange finish.

CONTENTS

INTRODUCTION

One of the most important systems in an underwater habitat or vehicle in terms of accomplishing a majority of missions is the viewport system. Reference 1 contains a complete listing of undersea vehicles and their viewport designs.

The objectives of this study are as follows:

1. To determine experimentally the structural response in terms of stresses and displacements of a typical full-scale viewport design.
2. To determine analytically the structural response of the same viewport design using the finite element method and to compare the results to the experimental results.
3. To determine the effect, if any, of the flange surface finish on the structural behavior of the viewport.

To adequately perform a stress analysis of the viewport design, a balanced format, consisting of both an experimental and an analytical approach, was followed. Results from the above format enable a better understanding of the true mechanical behavior of the viewport, thus allowing intelligent design modifications. Since the experimental results are taken from full-scale viewports during actual tests, they add credibility to the entire study and provide a check for the analytical results.

The analytical approach attempts to simulate the actual structure by idealizing both the structure and the boundary conditions. Comparison of the analytical results with the experimental results will serve to indicate the validity of the idealization. Once the analytical tool is verified, it can perform parametric studies on shapes, materials, and loading conditions to achieve optimum designs. These optimum designs are obtained much faster and more economically than by large-scale experimental programs.

Another cost advantage would be realized if the requirements on the flange surface finish could be safely relaxed. Many of the viewports in the vehicles today are lapped into 8 rms finished flanges to achieve a minimum of 80% contact surface area between the viewport and the seat. There are three economic disadvantages to this procedure. First, the viewport must be manually lapped into place; second, this procedure requires additional machining to achieve the smoother surface; and third, there is an absence of

interchangeability of the viewports due to the tight tolerances. The smoother surface finish does provide a lapped-joint seal for the viewport, but a much more economical seal design is possible and will be discussed in later studies.

DISCUSSION OF PARAMETERS

Acrylic plastic, which was first introduced as a material for hydrospace viewports in 1939 by Piccard,[2] was chosen for the viewport material in this study. There is a large accumulation of experience with this material as today more than 95% of the submersibles use acrylic plastic viewports. Of particular importance is its low modulus of elasticity and plastic flow characteristics which permit localized yielding and thus, a redistribution of stresses.

The 90^{o} conical shape was chosen because it offers a compromise between cylindrical viewports and spherical viewports in three different ways. First, in terms of strength (with equal thickness/minor diameter (t/d) ratios) they rank in order of descending strength: spherical, conical, and cylindrical, respectively.[1] Second, with respect to fabrication difficulty and thus cost, the order reverses itself. Third, in terms of visibility, the 90^{o} conical shape again ranks between the spherical with the largest viewing angle and the cylindrical with the smallest. An interesting point is that the conical shape is used more frequently than the other two combined and yet it is the most difficult of the three to analyze. Four full-scale, 90^{o} conical viewports are shown in Figure 1.

The strength of a viewport increases with an increase in the viewport-thickness/ minor-diameter ratio, t/d, with all other variables constrained. A typical viewport cross section is shown in Figure 2. A nominal t/d ratio of 0.5 was utilized in this study as this ratio represents a design for about a 6,000-foot-depth vehicle and would allow investigation of the continental shelf, continental slope, and bathyal regions. The depth zone 0 to 6,000 feet represents 16% of the area of all oceans.

DESIGN OF INVESTIGATION

The investigation was subdivided into three phases: (1) experimental investigation of a full-scale viewport design, (2) analytical investigation of the same viewport design, and (3) experimental studies on model viewports to determine the effect of different flange surface finishes.

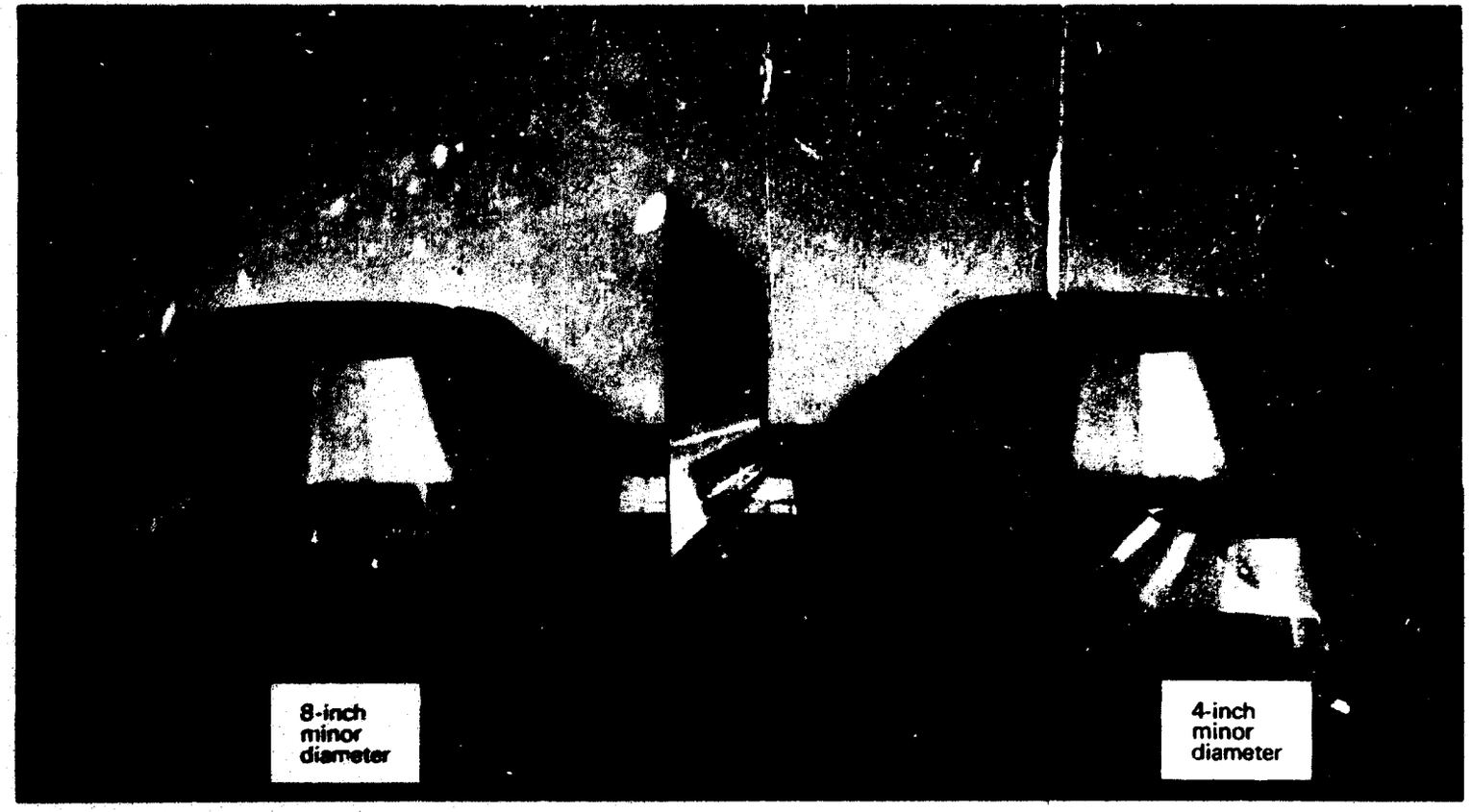

Figure 1. Full-scale, 90° conical, acrylic viewports with nominal t/d ratios of 0.5.

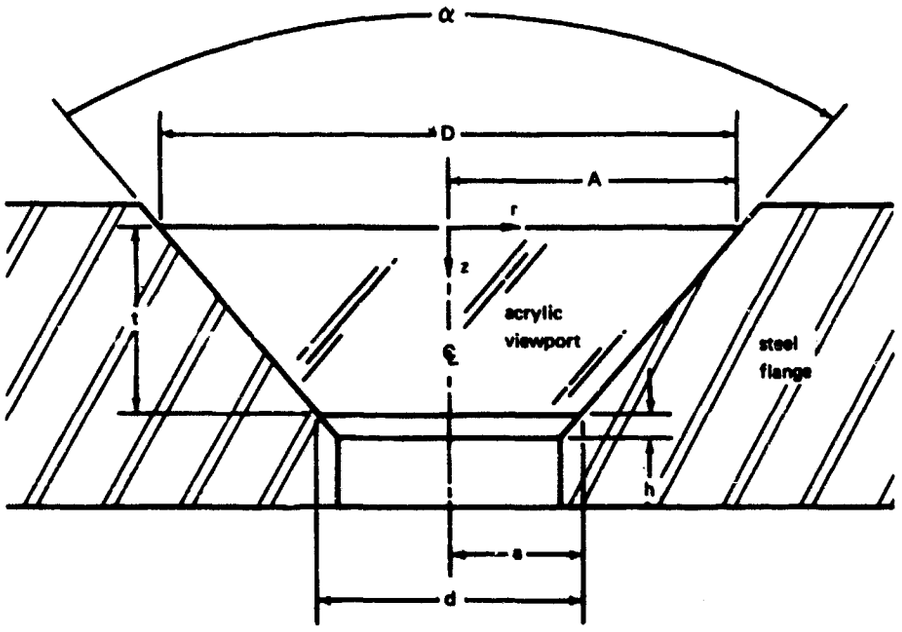

Figure 2. Cross section of a typical viewport.

Experimental Phase

Four viewports, as shown in Figure 1, were tested in the experimental phase; their dimensions are shown in Table 1. Note that there were two nominal sizes of the minor diameter, 4-inch and 8-inch. The four viewports were strain-gaged on both the high-pressure and low-pressure faces and tested to 8,000 psi, or about three times the operational pressure of 2,670 psi at 6,000 feet. The volume of the two viewport sizes differed by a factor of eight as this was done to investigate the scaling effect on the stress distribution.

Detailed information on the strain gage instrumentation, measurement of displacements, and reduction of data is presented in Appendix A. Appendix B contains descriptions of the high-pressure equipment, preparation of viewport specimens, and the test procedure.

The study of mechanical behavior cannot be easily separated from the material characteristics. The material properties, modulus of elasticity and Poisson's ratio, were necessary for both the strain-gage data reduction and the finite element method. As it was possible that the handbook values would yield incorrect results, these properties were measured experimentally as explained in Appendix C.

Table 1. Full-Scale Viewport Dimensions

Included Angle, α (deg ± 5 min)	Major Diameter, D (in.)	Minor Diameter, d (in.)	Thickness, t (in.)	t/d
Experimental Viewports				
90° 0′	16.107	8.503	3.802	0.447
90° 0′	16.098	8.500	3.799	0.447
90° 0′	8.271	4.251	2.010	0.473
90° 0′	8.273	4.257	2.008	0.472
Finite Element Viewport				
89°16′	16.200	8.500	3.900	0.459

Analytical Phase

A single viewport design, as listed in Table 1, was used in the analytical phase. The absolute dimensions of the finite element viewport design were arbitrarily chosen, except for the t/d ratio and included angle, which were equivalent to those for the experimental viewports. This did not impair the results in any way, because they are all presented in a nondimensional form. Detailed information on the finite element method is presented in Appendix D.

Two boundary conditions were used on the conical surface in this study as shown in Figure 3. Since the exact coefficient of friction was unknown at the viewport-flange interface, two extreme conditions were imposed, fixed and free. The fixed condition would represent an infinite coefficient of friction, while the free boundary condition would represent zero friction. In this way, the computer results should bracket the actual results. The loading condition on the high-pressure face was 1,000 psi pressure while the low-pressure face was left as a free boundary. Due to the axisymmetry of the viewport, the centerline was given the boundary condition of no radial displacement, but free axial displacement.

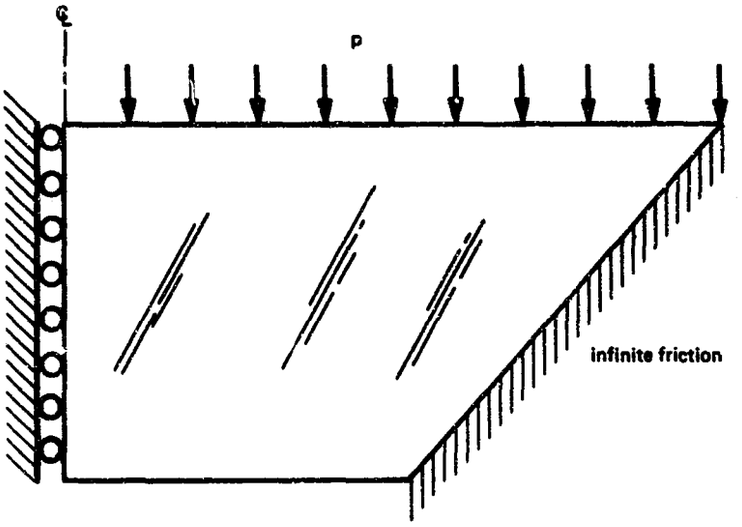

(a) Fixed boundary.

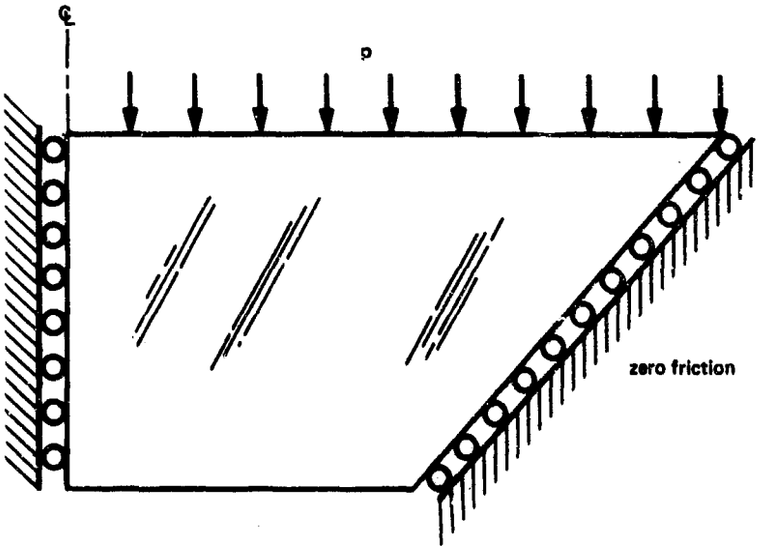

(b) Free boundary.

Figure 3. Boundary conditions for finite element analysis.

Flange Surface Finish Phase

The last stated objective of this study was to investigate the effects of the flange surface finish on the viewports. Both economic and time constraints prevented investigation of the experimental stresses in large viewports with varying flange surface finishes, so the experimentation was done with model viewports (nominal 1-inch minor diameter). A method was sought to vary only the one parameter, flange surface finish. Since the viewports could not be strain-gaged adequately because of their small size, it was felt that loading them into the plastic range would yield a qualitative, as opposed to a quantitative, answer.

Therefore, 15 identical model viewports were cycled five times to 23,000 psi. The viewports were tested three at a time in a specially built three-viewport flange. The seats in the flange each had a different surface finish, 32, 63, and 125 rms. Information on the model viewports, high-pressure equipment, test procedure, and post-test visual observations is presented in Appendix E.

RESULTS

Stresses and displacements from both the experimental and analytical studies are presented in this section. For the analytical study, two solutions are given corresponding to the two limiting boundary conditions, fixed and free. In addition, the effects of varying the flange surface finish are considered, based on the results of the model viewport tests. These results are compared to the experimental and analytical results.

Experimental and Analytical

The displacements and the stresses are both presented to gain a greater understanding of the mechanical behavior of the viewport design and for comparison between the experimental and analytical data. Nearly all the results are presented in a nondimensionalized form for use with any pressure or any diameter viewport with a 90° included angle and a nominal t/d ratio of 0.5.

Displacements. The experimental displacements are compared to the analytical displacements in Table 2. The comparisons are for selected locations on the low-pressure face which were determined by the dial indicator position. The fixed boundary displacements were less than the free

boundary case as was expected. It was not expected, however, that the experimental displacements would lie outside the analytical solution range. Reasons for this discrepancy are presented after the stress results are introduced.

Figure 4 shows the displaced shapes of the viewport for the two analytical boundary conditions, fixed and free. These plots provide a visual aid for understanding what movement the viewport experiences. The dots represent the initial shape of the viewport while the solid lines represent the displaced shape. Displacements of the individual nodal points enable the plot to be constructed. The displacements are not to scale so the value of the center displacement on the low-pressure face is shown and all other displacements can be evaluated relative to it.

Axial-direction displacement contour plots are shown in Figure 5 with the contours drawn through equal axial displacements. The contours are separated by equal increments of displacement, so gradients can be determined by the physical distances between contour lines. For example, a large gradient appears near the low-pressure face corner on both plots, and for the fixed boundary case the equal spacing of the contours on the high-pressure face indicates a constant gradient. For the fixed boundary case, the contours indicate that the viewport has displaced uniformly, but with the free boundary condition the viewport exhibited the effect of "plugging." Plugging is defined as the **z** displacement of the entire viewport with the **r-θ** planes remaining plane, which results in the inducement of compressive stresses.

Table 2. Low-Pressure Face Displacements
(per 1,000 psi in linear range)

Type of Displacement	$\delta_z/a \times 10^3$ at Locations—			
	r/a = 0.0	r/a = 0.5	r/a = 0.9	r/a = 1.0
Experimental	4.60	4.04	2.50	—[a]
Analytical (free boundary)	4.52	3.93	2.38	1.41
Analytical (fixed boundary)	3.51	2.82	1.06	0.0

[a] No measurement at this location.

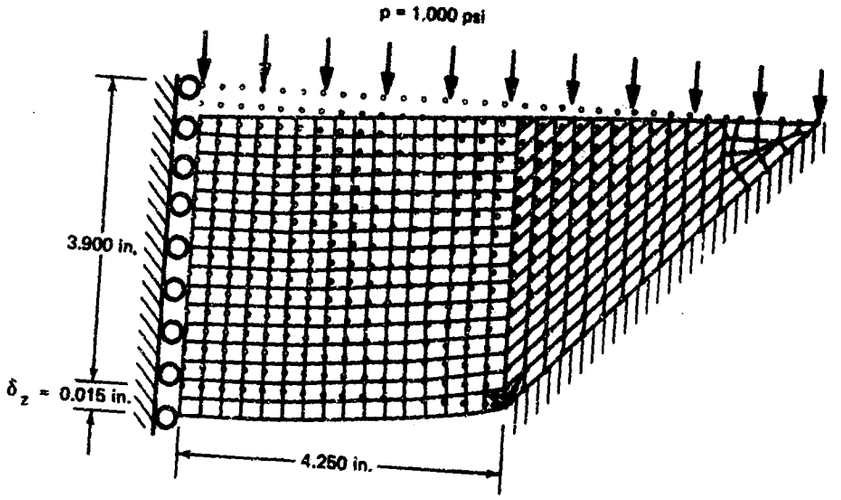

(a) Fixed boundary.

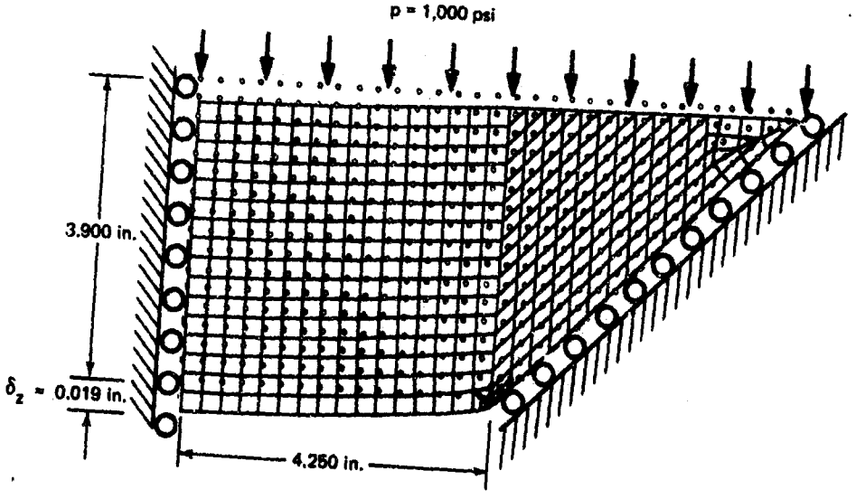

(b) Free boundary.

Figure 4. Displaced shapes of viewport.

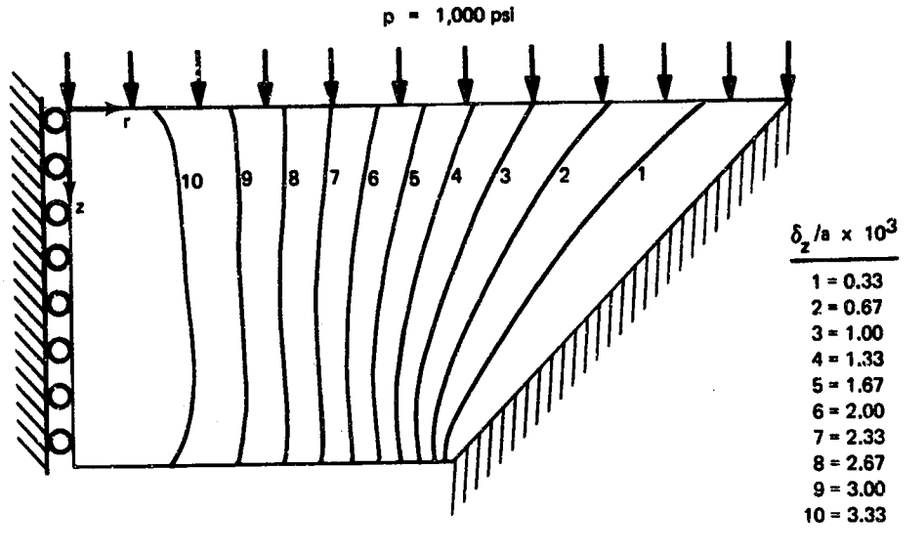

(a) Fixed boundary.

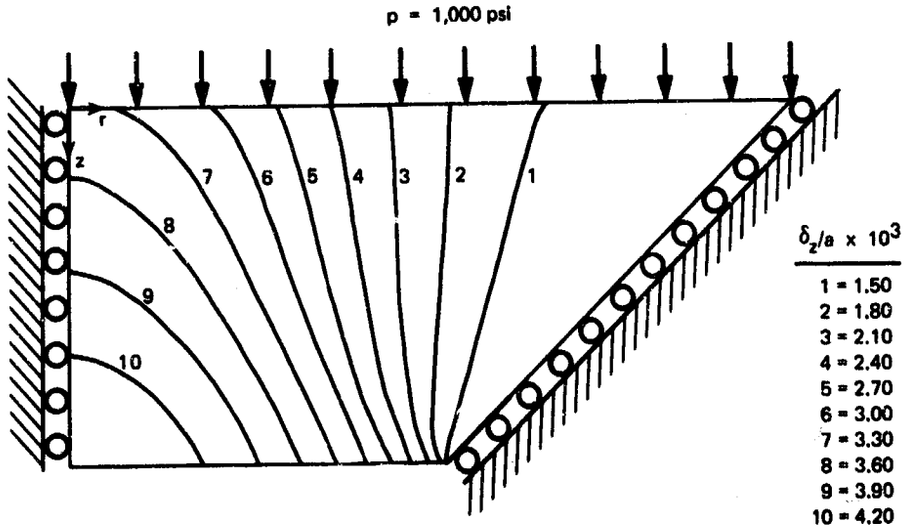

(b) Free boundary.

Figure 5. Axial displacement contour plots.

The radial displacement contour plots are shown in Figure 6. In the fixed boundary case, the contour parallel to the conical face is indicative of the imposed boundary condition. The change in sign of the radial displacements substantiates the presence of a "plate-type" flexural bending. The contours in the free boundary case indicate that the plugging action has supplanted the bending action which was present in the fixed case.

Stresses. The experimental surface stresses, both radial and tangential, on the high-pressure face are compared to the analytical results in Figure 7. The radial and tangential stress distributions for both the experimental and analytical cases are in compression as was expected due to the pressure loading on that face. The experimental stress distribution is bracketed by the two analytical cases because the experimental viewports were neither perfectly fixed nor perfectly free; rather they had some nominal coefficient of friction at the viewport-flange interface. For the analytical results, the fixed case stress distribution is the lowest in magnitude with the radial stress approaching zero at the edge, while the free boundary case had the highest stress magnitude. It appears that the stress increase over the fixed case was due to the plugging action. The radial stress for the free case was 25% higher than the fixed case at the centerline. Both the free and fixed case curves remain parallel across the entire high-pressure face.

The experimental surface stresses, both radial and tangential, on the low-pressure face are compared to the analytical results in Figure 8. With the experimental viewport in a flange with a relatively smooth finish of 32 rms, the experimental viewport underwent some plugging as evidenced by the experimental stress distribution curve remaining compressive. For the analytical cases, the fixed case went into tension on this face due to the bending while the free case remained in compression. The analytical cases again bracketed the experimental case. All stress distributions indicate a high stress concentration at the low-pressure face corner. The value of the maximum linear elastic stress at this point is probably infinity due to the sharp corner. The analytical curves, both free and fixed, remain parallel to one another on this face also. In the actual viewport, there will be some minimal amount of plastic flow at the low-pressure face corner location immediately upon loading. This demonstrates how advantageous the ductility of acrylic plastic is when used as a material for conical viewports.

The analytical internal stress distributions for the two extreme boundary conditions are shown in Figures 9, 10, and 11, for radial, tangential, and axial, respectively. In these same figures, some of the contours were eliminated at the low-pressure face corners due to congestion.

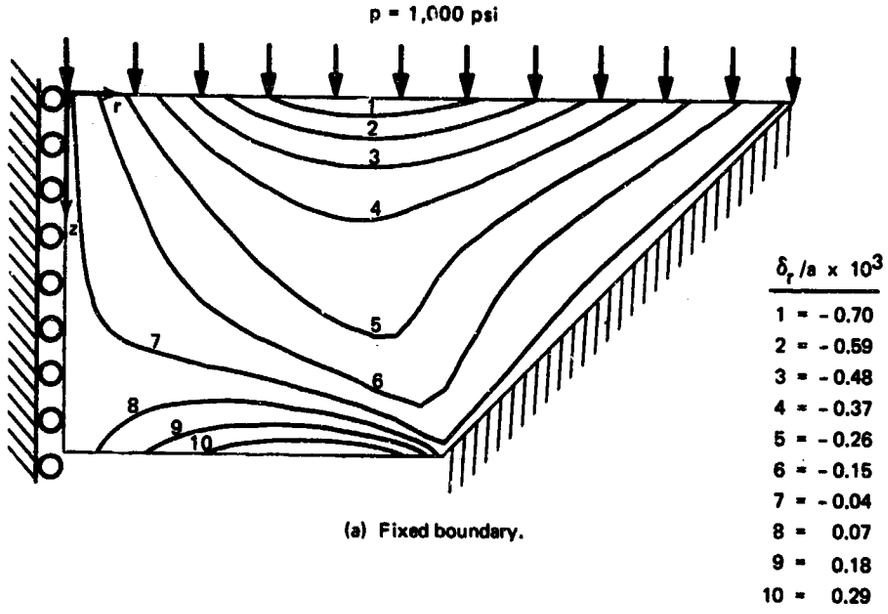

(a) Fixed boundary.

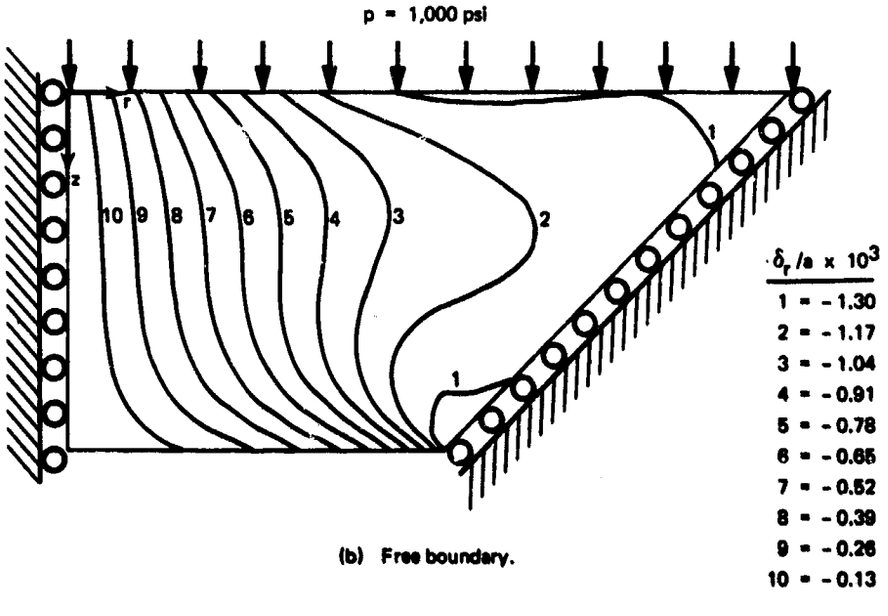

(b) Free boundary.

Figure 6. Radial displacement contour plots.

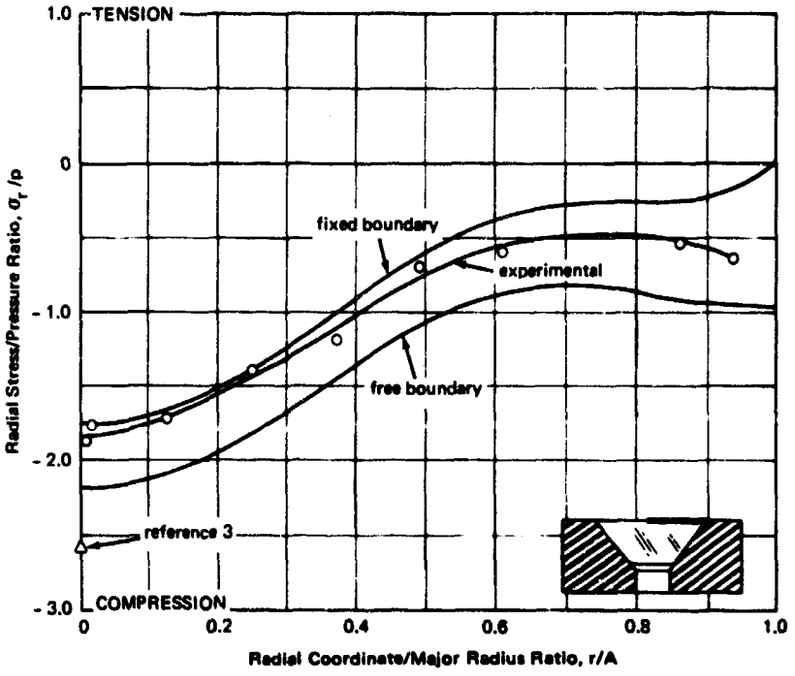

(a) Radial stress.

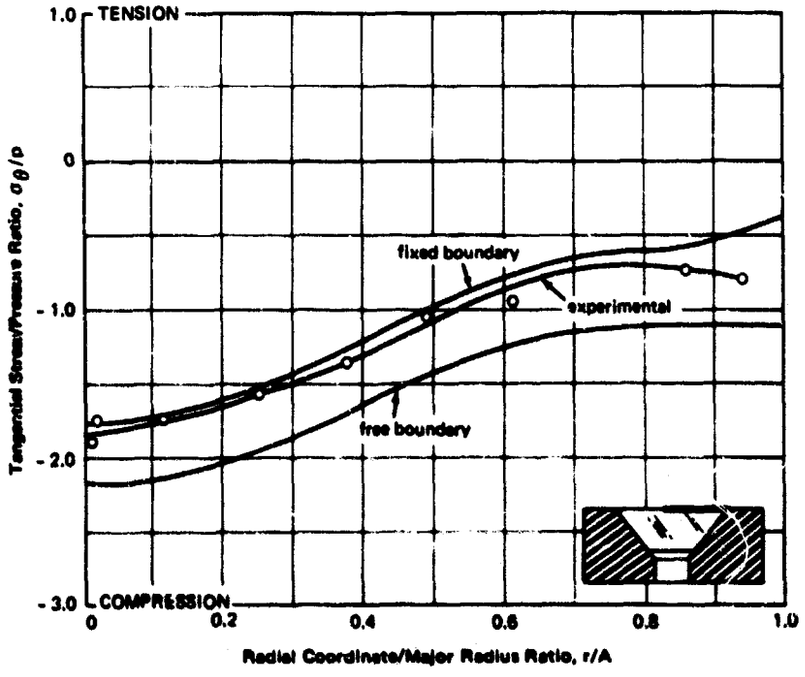

(b) Tangential stress.

Figure 7. Stress distribution on high-pressure face.

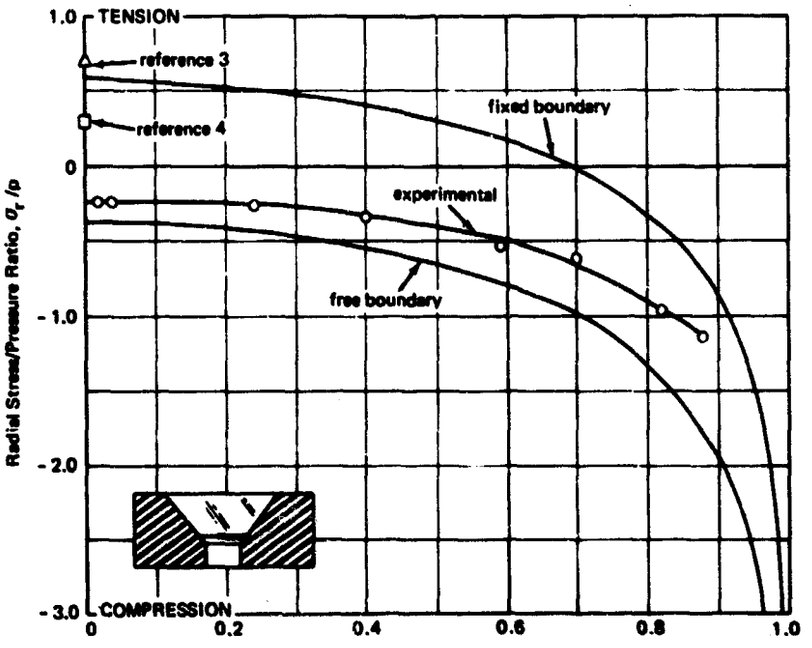

(a) Radial stress.

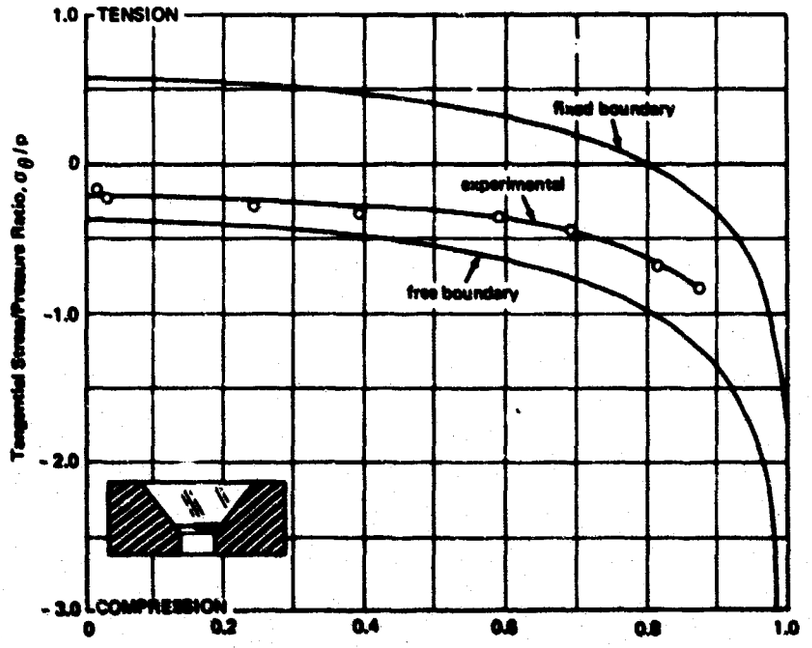

(b) Tangential stress.

Figure 8. Stress distribution on low-pressure face.

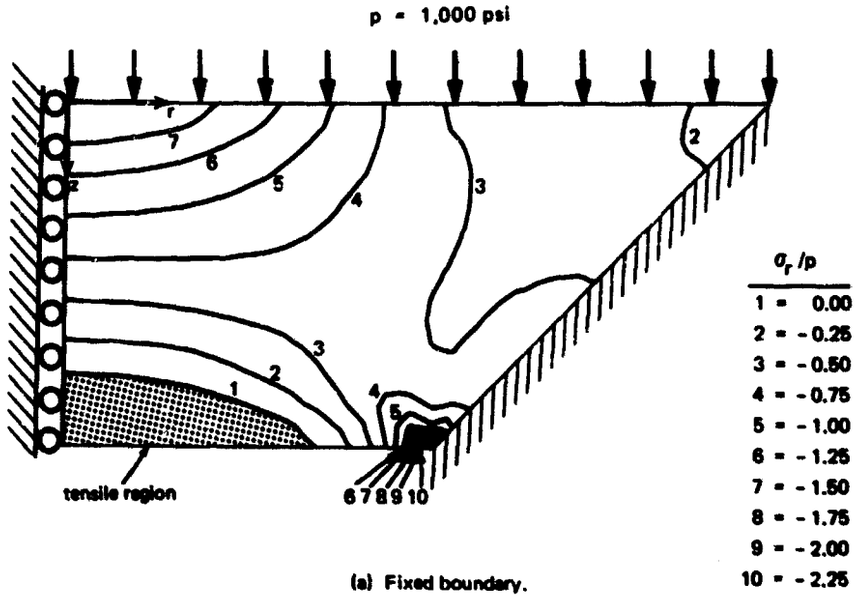

(a) Fixed boundary.

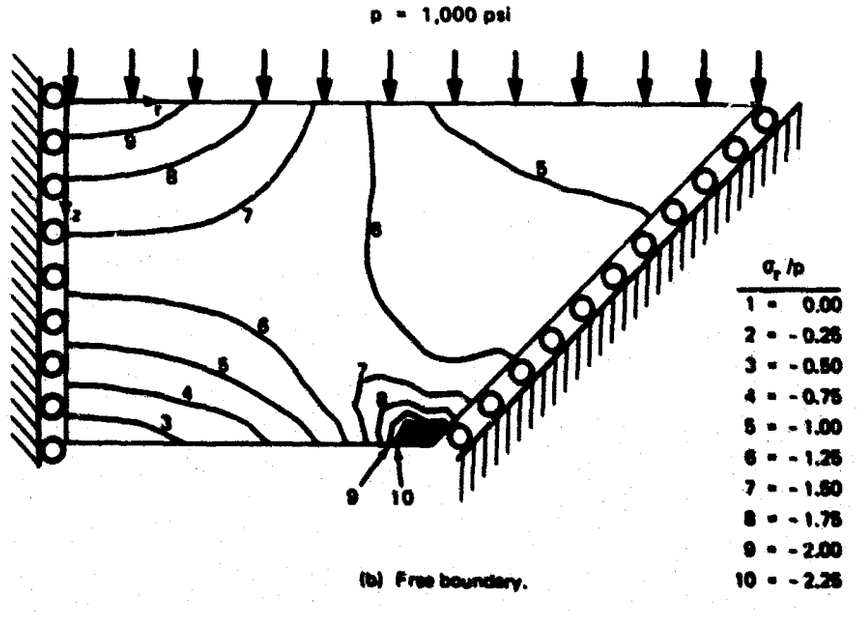

(b) Free boundary.

Figure 9. Radial stress contour plots.

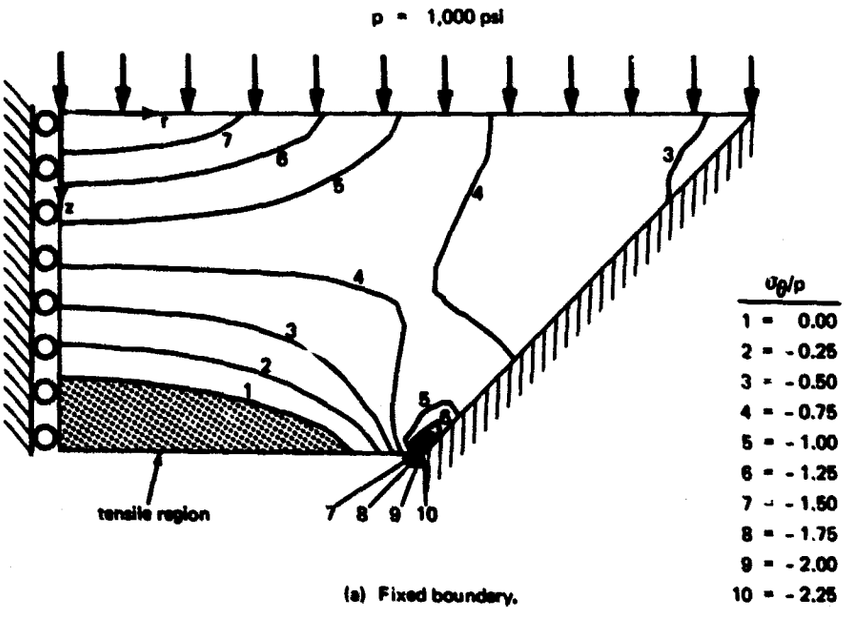

σ_θ/p	
1	0.00
2	- 0.25
3	- 0.50
4	- 0.75
5	- 1.00
6	- 1.25
7	- 1.50
8	- 1.75
9	- 2.00
10	- 2.25

(a) Fixed boundary.

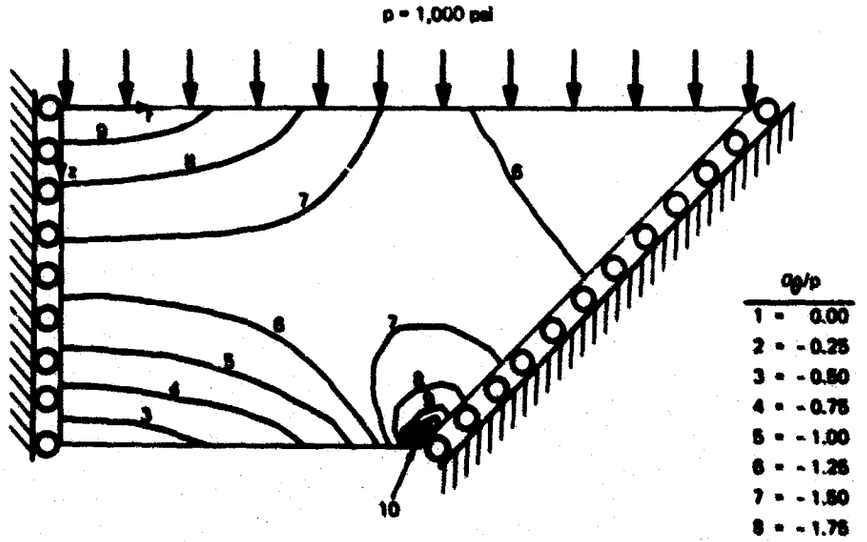

σ_θ/p	
1	0.00
2	- 0.25
3	- 0.50
4	- 0.75
5	- 1.00
6	- 1.25
7	- 1.50
8	- 1.75
9	- 2.00
10	- 2.25

(b) Free boundary.

Figure 10. Tangential stress contour plots.

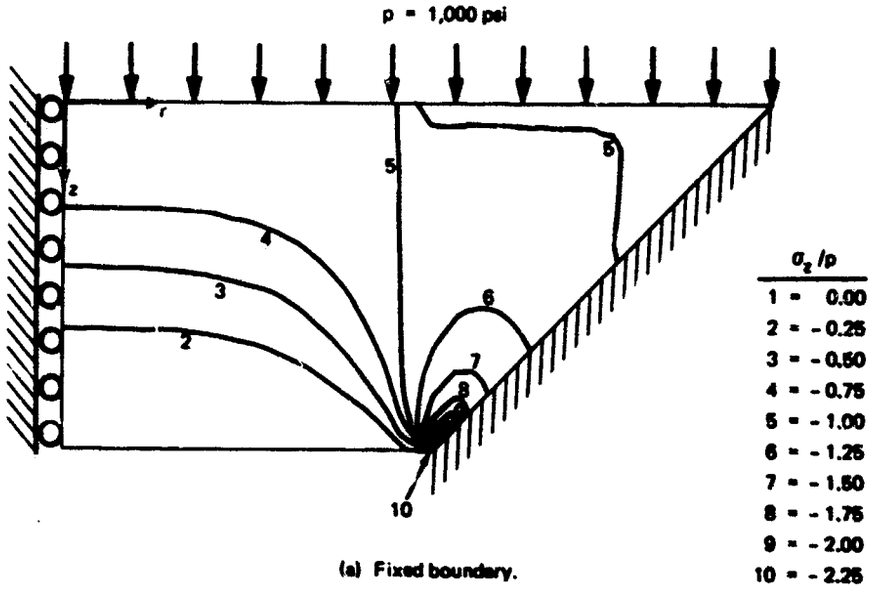

(a) Fixed boundary.

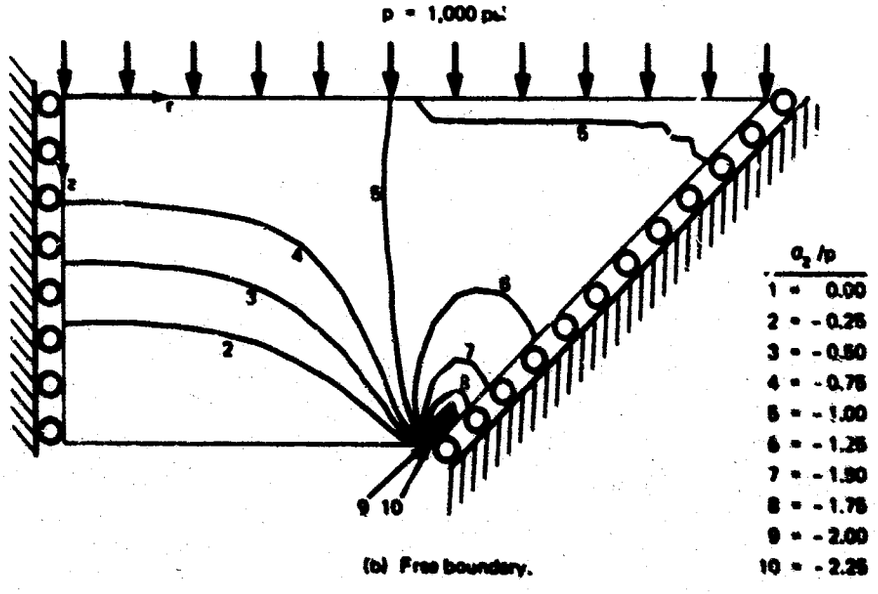

(b) Free boundary.

Figure 11. Axial stress contour plots.

In Figures 9 and 10, the contour plots for the fixed and free cases are similar in pattern except for the shift in stress magnitudes. The changes near the low-pressure face are particularly noteworthy as they show the change from compression to tension. Figure 11 shows the axial stress contour plots for both boundary conditions. The stress distribution for both cases is essentially equal as would be expected due to the axial pressure load. The only difference appears at the high-pressure face corner where the boundary condition does manage to influence the stresses.

Effects of Flange Surface Finish

Typical cross sections of the model viewports after test are shown in Figure 12, where the damage is an average of the actual test results. More detailed descriptions of the model viewports after testing are included in Appendix E. Figure 12 indicates that as the surface finish ranged from the rough 125 rms finish to the smooth 32 rms finish, the magnitude of the gross damage increased. More quantitative results are given in Table 3, which lists the values of the depression (crater) depths and the permanent extrusions.

Table 3. Post-Test Measurements of Model Viewports

Flange Finish (rms)	Set Number					Average
	1	2	3	4	5	
Low-Pressure Face Permanent Extrusion (in.)						
125	0.025	0.030	0.038	0.037	0.025	0.031
63	0.064	0.055	0.069	0.080	0.058	0.065
32	0.070	0.060	0.078	0.085	0.064	0.071
High-Pressure Face Depression Depth (in.)						
125	0.004	0.005	0.008	0.007	0.003	0.005
63	0.029	0.015	0.032	0.036	0.016	0.026
32	0.035	0.023	0.040	0.042	0.026	0.033

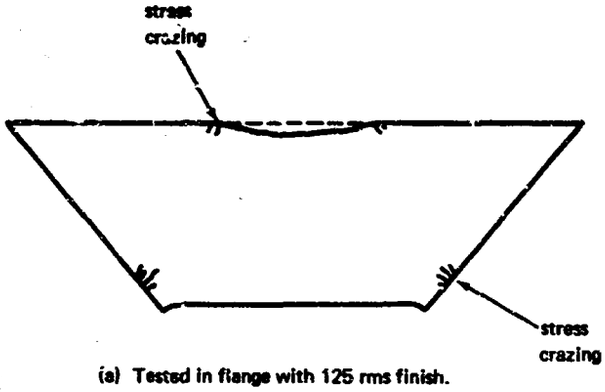

(a) Tested in flange with 125 rms finish.

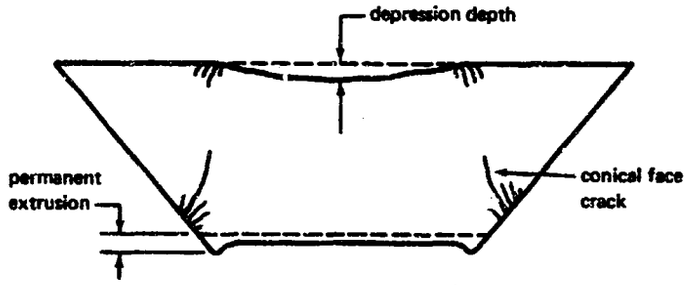

(b) Tested in flange with 63 rms finish.

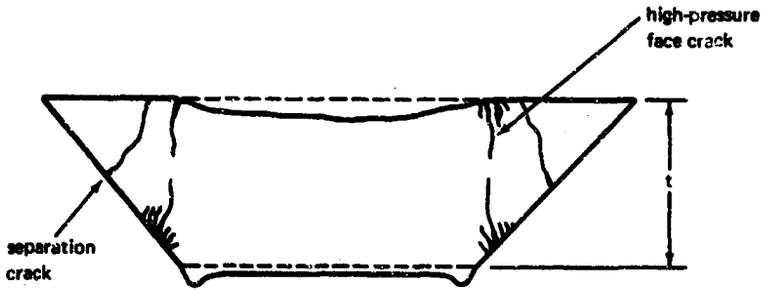

(c) Tested in flange with 32 rms finish.

Figure 12. Cross sections of model viewports showing locations of damage.

It appears from the data in the model viewport study that two statements can be made: (1) cracks and crazing always appear near a region of plastic flow; and (2) as the plastic flow increases, the cracks become deeper and more numerous. Since these tests were run quickly to reduce creep, the plastic flow was essentially due to high stress levels. The cracks were dependent on the stress level in this study, but as with all viscoelastic materials the total deformation or total strain is what is important.

In general, then, cracks were caused by high stress levels. The stress crazing around the crater located on the high-pressure face was probably due to plastic flow or the pulling away of material in the crater. A similar action would have occurred at the low-pressure face corner where the material yielded and the yielded portion attempted to pull away from the remainder of the viewport.

It is possible that some of the cracking in the viewports was due to extension of the low-pressure face beyond the conical flange. It must be pointed out, however, that for this to happen, the plastic flow must have been of such a magnitude as to allow the viewport to move down the flange to this point. As shown in Table 4, the model viewports were elevated in their flanges the same proportional amount as were the full-scale viewports. In this respect, the only difference in the full-scale and model tests was the pressure loading, where the models were tested to approximately three times the load on the full-scale viewports.

The two results, post-test visual observations and measured changes in dimensions, imply direct agreement with the analytical results previously discussed; namely, lower stress levels occur in the given viewport design when the boundary is fixed (125 rms) than when it is free (32 rms). The model viewports also verified the locations of the points of high stress concentration: center of the high-pressure face and corner of the low-pressure face.

DISCUSSION

The discussion is subdivided into three sections: (1) experimental and analytical stress analysis phase, (2) other published work on viewport stress analysis, and (3) effect of flange surface finish on the viewport in terms of the stress analysis and model viewport results.

Table 4. Viewport-Flange Diameter and Angle Mismatches

a. Full-Scale Viewports

Minor Diameter, d (in.)	Elevation in Flange, h (in.)	h/d x 10^2	Viewport-Flange Angle Mismatch[a] (minutes)
8.503	0.255	3.00	0
8 500	0.253	2.98	0
4.251	0.129	3.03	0
4.257	0.132	3.10	0

b. Model Viewports[b]

Set Number	Flange Finish (rms)	Elevation in Flange, h (in.)	h/d x 10^2	Viewport-Flange Angle Mismatch[a] (minutes)
1	125	0.030	2.84	20
	63	0.028	2.75	0
	32	0.029	2.73	30
2	125	0.028	2.68	20
	63	0.026	2.46	-10
	32	0.029	2.72	20
3	125	0.032	3.00	30
	63	0.028	2.75	0
	32	0.025	2.38	10
4	125	0.029	2.75	20
	63	0.026	2.46	0
	32	0.029	2.73	30
5	125	0.028	2.65	0
	63	0.025	2.36	10
	32	0.025	2.36	0

[a] Angle mismatch ± 10 minutes.

[b] Viewports randomly selected to form the sets.

Experimental and Analytical

As previously demonstrated, the experimental stresses were successfully bracketed by the analytical stresses of the finite element solutions. However, the experimental displacements slightly exceed the solution range of the analytical model (Table 2). This slight discrepancy was probably due in part to (1) compaction and excretion of silicone grease at the viewport-flange interface, and (2) slight viewport-flange angle mismatch causing small localized yielding and thus larger displacements.

Experimental displacement readings were not taken at the edge of the low-pressure face because the viewport was elevated; thus, the flange protruded over the low-pressure face (Figure 2). A similar difficulty presented itself when measuring strains on both faces of the viewports. It was almost physically impossible to mount gages right at the viewport edge, hence, the absence of experimental stresses near the edges in Figures 7 and 8.

Based on the stress distribution results, the stress concentration at the low-pressure face corner was much greater than that at the center of the high-pressure face. This fact means that the stress at the low-pressure face corner probably determines the viewport's operational depth. It is known that the corner tip plastically flows to redistribute the stresses, because all of the full-scale viewports exhibited rounded-off low-pressure face corners upon post-test visual inspection. The question appears to be, therefore, just how much plastic flow can be tolerated at the corner? Any plastic flow at the other stress concentration location, the center of the high-pressure face, is, of course, intolerable from a visibility standpoint. A more thorough discussion of failure will be provided in later studies.

Other Published Work

Winter and Becker[3] obtained the points in Figure 7a and 8a (identified as "reference 3" points) using three-dimensional photoelasticity. They tested several 90° viewports with a range of **t/d** ratios; the points in the figures were taken from their experimental data plot. The viewport material was an epoxy, Hysol-4290, and was machined to a 32 rms finish. The models were coated with a thin layer of VISCASIL-5000 silicone fluid before placement in a flange which had a 32 rms finish. The model viewports were stress frozen at 300°F and a thin, flat slice then was cut from the center for the analysis. No attempt was made to get a complete internal stress solution, as the only internal solution given was along the centerline axis.

Winter[4] achieved the datum point in Figure 8a (identified as "reference 4" point) with the use of a strain gage located at the center of the low-pressure face. His tests were run at room temperature with a pressurization rate of about 1,000 psi/min and both the model viewports and the flange had a surface finish of 16 rms. Winter did not test a model viewport with an equivalent geometry, but he did present a curve for 90° viewports with a range of **t/d** ratios. He utilized a foil strain gage and the values of 455,000 psi for the modulus of elasticity and 0.35 for Poisson's ratio.

As noted by Winter, the possibility of inaccurate results in Reference 3 was high due to the substitution of epoxy for acrylic. Although acrylic is a photoelastic material, the epoxy was used because of its higher sensitivity or lower fringe value. Two problems were created when the epoxy replaced the acrylic in the stress-freezing, three-dimensional photoelastic analysis. First, the elastic stress distribution is not independent of Poisson's ratio in a three-dimensional analysis. Usually, any error due to the differences between Poisson's ratio for models and prototypes can be neglected, but it is possible that the high value of Poisson's ratio, approaching 0.5, for the epoxy was significant in this instance. Second, it is quite possible that the coefficient of friction for the 300°F epoxy-steel flange interface was different than the coefficient for room-temperature acrylic and a steel flange. A stress-freezing temperature must be employed in the three-dimensional photoelastic analysis although it does introduce another parameter which can be significant.

Effects of Flange Surface Finish

The results in Table 3 had variations, although the viewports were all cut from the same sheet of acrylic. Since all parameters were held constant within the sets, these variations were due to random factors only and did not have any effect on the results. The possible variations were viewport-flange mismatches of diameters and included angles (Table 4) due to the tolerances on dimensions. Another possible variation was the amount of grease applied to the viewports before the test. The possible variations between sets were pressure and temperature, but as indicated, these effects were nullified within the sets.

To satisfy the third objective, model viewports were tested in flanges of different surface finishes to determine the effects on structural response. These viewports could have been tested to a higher static pressure and perhaps achieved the same objective, but this would not have answered the questions about the interrelationships of cycling, surface roughness, and crack initiation. The cycling aspect is important because as the vehicles return to the surface, the pressure returns to zero and the viewport relaxes.

At first, one might hypothesize that the rougher flange finish would have a deleterious effect on the acrylic by initiating cracks at the numerous points of high stress concentration. No evidence was present to substantiate this hypothesis. In fact, as was shown, the viewport in the roughest flange actually suffered less damage due to cracking. It is believed the following two reasons contributed to the independence of crack initiation and surface finish. First, the low modulus and ductility of acrylic allowed it to plastically flow at the points of high stress, thus the presence of embossing on the conical surface (Figure E-3 in Appendix E). The net effect was only to increase the coefficient of friction at the viewport-flange interface, thereby restraining the viewport from axial movement. Second, the stresses in the viewport at the viewport-flange interface were always compressive. It should be pointed out, however, that when in tension, acrylic is quite susceptible to stress concentrations and can fail in brittle modes similar to glass. There is, of course, an upper limit to the roughness of the flange finish. It is unknown from the results of this study what the maximum safe value might be; only that the value of 125 rms falls within the safe range.

It appears, then, that the rougher surface finish for this particular viewport design decreases stress levels besides reducing the machining cost of the flange. There is a disadvantage, however, as the compressive stress on the low-pressure face goes to tension. Maximum working tensile stresses of 2,000 to 3,000 psi are recommended because with sustained higher tensile stresses, acrylic develops crazing.[5] In fact, acrylic is used as a model material in experimental stress analysis where the crazing is an indicator of maximum tensile stresses. The fine hairline cracks called stress crazing develop normal to the tensile stresses just as with brittle coatings. In acrylic, the stress crazing is a first indication of incipient failure.

Any stress crazing on the low-pressure face would, of course, obliterate visibility. So, applying a working stress value of 2,500 psi (ultimate tensile strength 10,500) to this viewport design, it was found that the design is safe from crazing if operated at a pressure less than 4,400 psi or 9,900 feet.

FINDINGS

The results in this study, on a nominal $t/d = 0.5$, 90° conical, acrylic plastic viewport, indicate that:

1. The viewport experiences both plugging and bending behavior; more bending occurring with the fixed boundary.

2. The viewport has two points of high stress levels, the center of the high-pressure face and the low-pressure face corner.

3. The viewports, with a volume ratio of eight, exhibited no scaling effects with either the displacements or the stresses (Appendix A).

4. The modulus of elasticity was found to equal 444,000 psi; Poisson's ratio, 0.4; and the bulk modulus of elasticity, 740,000 psi (Appendix C).

CONCLUSIONS

1. The finite element method can successfully bracket the elastic stress distribution incurred by a viewport during service by using two boundary conditions, fixed and free. With this analytical capability, the designer can now perform parametric studies to determine optimum viewport designs in a faster and more economical manner as compared to large-scale experimental programs. This enables a concentration of experimental tests on the optimum designs.

2. The roughness of the flange surface significantly affects the viewport stress distribution. As the flange surface finish tends from smooth to rough, the critical stresses in the viewport are reduced. Therefore, based on a structural analysis of the viewport design in this study, the 8 to 32 rms requirement for viewport flanges can be safely relaxed to 125 rms, thus resulting in a more economic viewport installation.

RECOMMENDATIONS

1. Determine design curves for conical viewports with different t/d ratios and included angles by using the finite element method and a failure criterion for acrylic.

2. Continue investigation of the friction effect at the viewport-flange interface by using both experimental and finite element techniques in an attempt to predict the true response.

3. Determine the effects of viewport-flange angle mismatches on the structural response of a viewport by comparing experimental and analytical results.

ACKNOWLEDGMENT

Mr. John McKay instrumented the full-scale viewports and conducted the experimental tests.

Appendix A

INSTRUMENTATION AND DATA REDUCTION FOR EXPERIMENTAL PHASE

INTRODUCTION

The first objective of this study was to determine experimentally the stresses and displacements of the four conical acrylic viewports shown in Figure 1. Resulting stress distributions would also be available for comparison with the results of the finite element analysis. Strain gages were chosen as the experimental method, even though only surface stresses could be achieved, because the gages would record the strains while the viewports were under actual conditions.

SCOPE OF INVESTIGATION

Sixty-eight, two-gage rosettes or 136 total strain gages were mounted on the faces of the four viewports as indicated in Figure A-1. The gages were located in this manner to provide the best coverage of the strain gradients. Each of the viewports, in turn, was pressurized to 8,000 psi at 500 psi/min. Strain gage readings were taken at every 1,000-psi increment. Dial indicators were used on the low-pressure faces to measure the viewport displacements. Due to the large number of calculations, the strain data were reduced and plotted with a computer code.

INSTRUMENTATION

Dial Indicators

Lufkin dial indicators with graduations of 0.001 inch were used on the low-pressure faces. The indicators were attached to the steel pressure vessels with magnetic bases as shown in Figure A-2. This method provided a positive means for recording the deflections of the viewports relative to the vessel. The dial indicators were spaced across a diameter with redundant locations so the readings could be averaged and also to determine if the viewports seated properly. The displacements were normalized for all four viewports; the results are shown in Figure A-3.

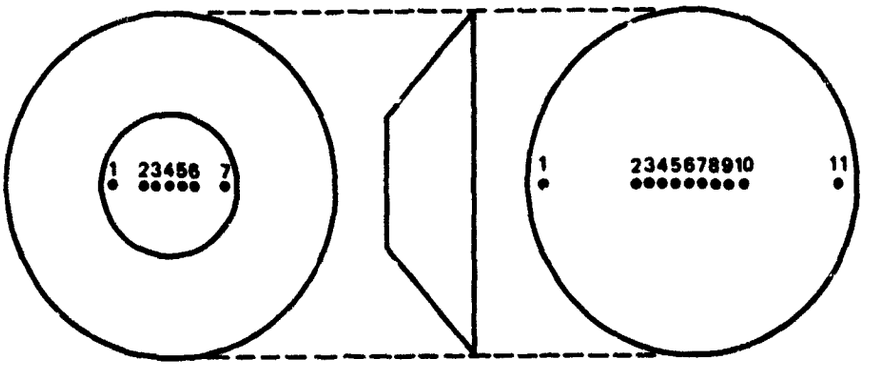

Rosette Locations—Pattern One			
Low-Pressure Face		High-Pressure Face	
r/a	Rosette Number	r/A	Rosette Number
0.016[a]	4	0.008[c]	6
0.032[b]	4	0.016[d]	6
0.240	3,5	0.123	5,7
0.397	2,6	0.248	4,8
0.875	1,7	0.373	3,9
		0.490	2,10
		0.940	1,11

[a] d = 8 inches
[b] d = 4 inches
[c] D = 16 inches
[d] D = 8 inches

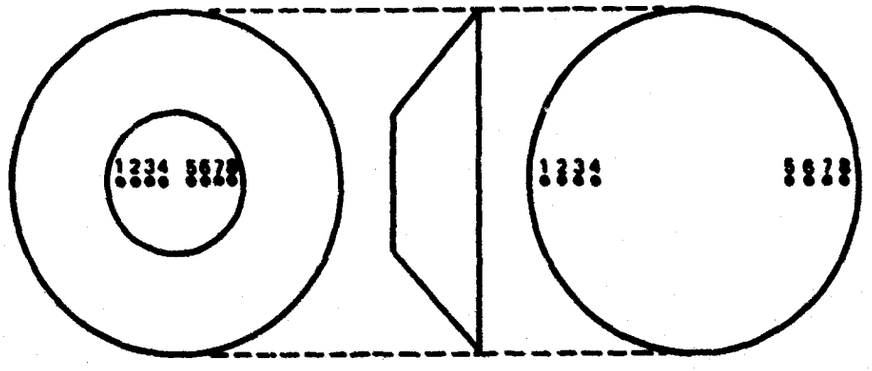

Rosette Locations—Pattern Two			
Low-Pressure Face		High-Pressure Face	
r/a	Rosette Number	r/A	Rosette Number
0.590	4,5	0.490	4,5
0.695	3,6	0.610	3,6
0.815	2,7	0.880	2,7
0.875	1,8	0.940	1,8

Figure A-1. Strain gage locations.

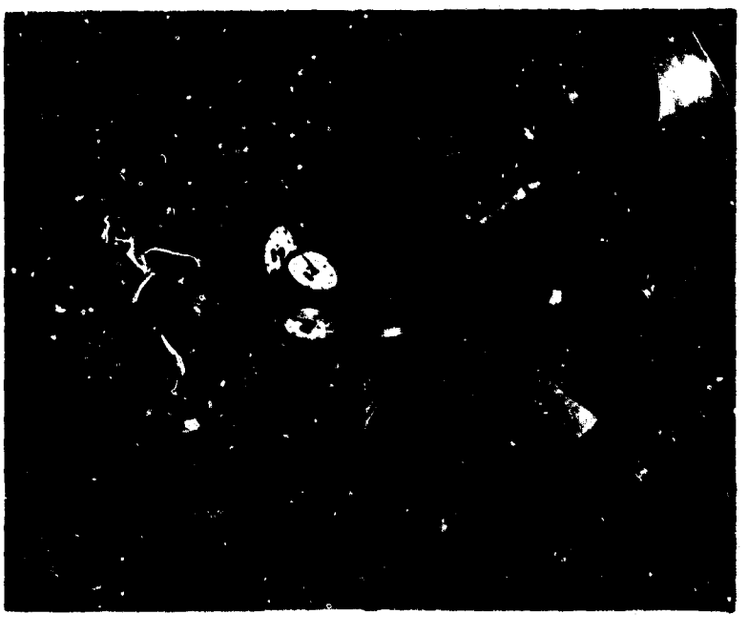

Figure A-2. Instrumentation for measurement of displacements.

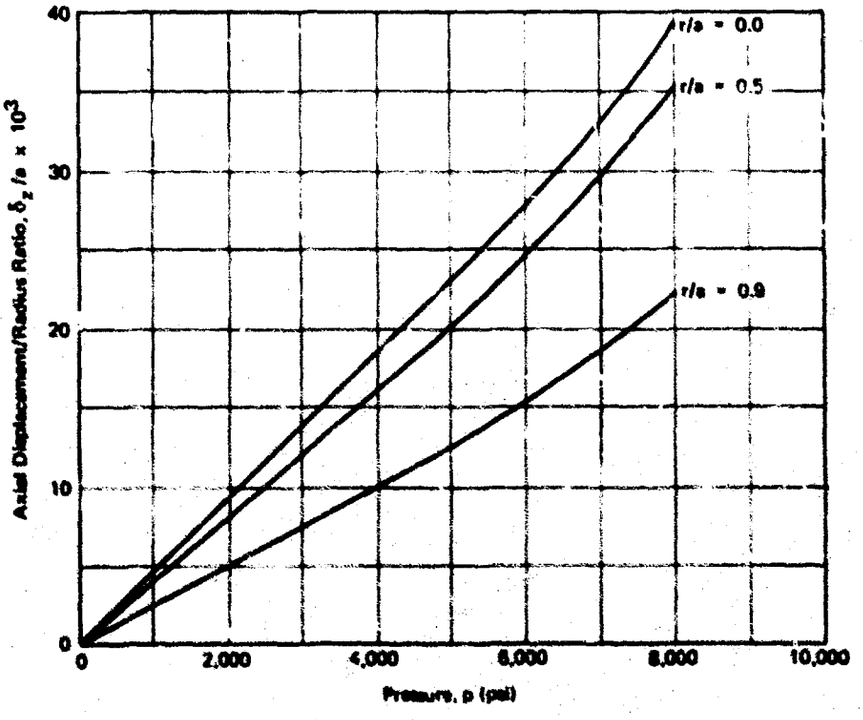

Figure A-3. Experimental displacements for low-pressure face.

Strain Gages

Two-gage, 90°, rectangular rosettes were used in this study due to the axisymmetry of the viewport. The constantan foil gages with epoxy backings were Baldwin-Lima-Hamilton FAET-12A-35S13WL, which have 350 ohms resistance and a 1/8-inch gage length. The small gage length was chosen to allow more gages on the viewport face in an attempt to capture the true strain gradient. The higher resistance of 350 ohms as opposed to the more common 120 ohms was chosen to reduce the heat dissipated by the gage. The gages were purchased with the leads already soldered to the gage tabs to preclude the heating of the plastic viewport by the soldering iron.

The acrylic viewports were cleaned with 99% isopropyl alcohol, wiped, and air dried. The gages were then attached to the acrylic with Eastman 910 adhesive, utilizing standard procedure. Strain gages mounted on 8-inch minor diameter viewports are shown in Figure A-4. General Electric RTV-108 was utilized for the waterproofing and mechanical protective agent. A half-bridge circuit was employed with a dummy temperature compensation gage located external to the high-pressure medium, and a Budd DATRAN unit with a digital readout was used for data recording. High-pressure, electrical penetrators, custom fabricated by Electro Oceanics, and having a pressure rating of 10,000 psi, were employed to transmit the data through the high-pressure interface. Three penetrators with sixteen 24-AWG conductors each were used with each test as shown in Figure A-5.

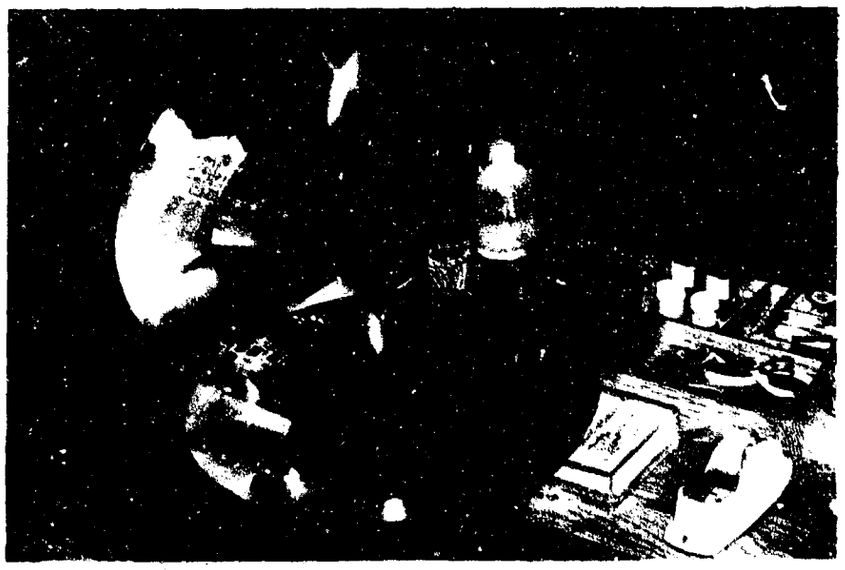

Figure A-4. Strain gages on 8-inch minor diameter viewports.

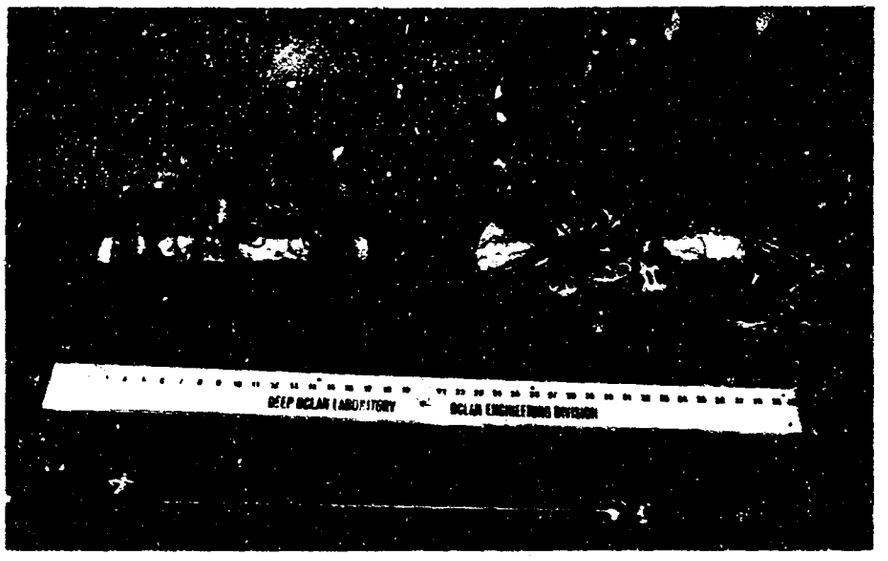

Figure A-5. High-pressure electrical penetrators shown with 8-inch minor diameter viewports.

REDUCTION OF STRAIN GAGE DATA

The first step in reducing the raw strain gage data was to convert the readings or apparent strains into true strains. With the gages at right angles to one another, the true strains could be found from the following equations[6]

$$\left.\begin{aligned} \epsilon_r &= \frac{(1-0.285K)(\epsilon_r' - K\epsilon_\theta')}{1-K^2} \\ \epsilon_\theta &= \frac{(1-0.285K)(\epsilon_\theta' - K\epsilon_r')}{1-K^2} \end{aligned}\right\} \quad \text{(A-1)}$$

where $\epsilon_r, \epsilon_\theta$ = radial and tangential true normal strains (in./in.)
K = transverse sensitivity of strain gage
$\epsilon_r', \epsilon_\theta'$ = radial and tangential apparent normal strains (in./in.)

and where 0.285 is the Poisson's ratio assumed by the manufacturer for use in calculating the stipulated gage factor which was input to the DATRAN unit. The above equations correct for the transverse sensitivity in the biaxial strain field and also for the difference in Poisson's ratio.

The three general constitutive equations[7]

$$\sigma_r = \frac{E}{(1+\nu)(1-2\nu)}\left[(1-\nu)\,\epsilon_r + \nu(\epsilon_\theta + \epsilon_z)\right] \qquad \text{(A-2)}$$

$$\sigma_\theta = \frac{E}{(1+\nu)(1-2\nu)}\left[(1-\nu)\,\epsilon_\theta + \nu(\epsilon_r + \epsilon_z)\right] \qquad \text{(A-3)}$$

$$\sigma_z = \frac{E}{(1+\nu)(1-2\nu)}\left[(1-\nu)\,\epsilon_z + \nu(\epsilon_r + \epsilon_\theta)\right] \qquad \text{(A-4)}$$

where $\sigma_r, \sigma_\theta, \sigma_z$ = radial, tangential, and axial normal stresses (psi)

E = modulus of elasticity (psi)

ν = Poisson's ratio

ϵ_z = true axial strain (in./in.)

were then utilized to find the radial and tangential stresses. The known quantities at this stage were ϵ_r, ϵ_θ, and the applied pressure, -p. The axial strain ϵ_z was then found from Equation A-4 by substitution of ϵ_r, ϵ_θ, and σ_z = -p and the rearrangement of terms

$$\epsilon_z = \frac{-p\,(1+\nu)(1-2\nu)}{E\,(1-\nu)} - \frac{\nu\,(\epsilon_r + \epsilon_\theta)}{1-\nu} \qquad \text{(A-5)}$$

The two stresses σ_r and σ_θ were then found from Equations A-2 and A-3.

For the low-pressure face, Equations A-2, A-3, and A-4 simplified to

$$\left.\begin{aligned} \sigma_r &= \frac{E\,(\epsilon_r + \nu\,\epsilon_\theta)}{1-\nu^2} \\ \sigma_\theta &= \frac{E\,(\epsilon_\theta + \nu\,\epsilon_r)}{1-\nu^2} \end{aligned}\right\} \qquad \text{(A-6)}$$

because $\sigma_z = 0$. All calculations were performed utilizing the values for E and ν as found in Appendix C.

Using the General Dynamics SC 4020 Plotter,[8] stress versus pressure plots were made for each rosette location on the viewport. A typical plot for r/A = 0.123, one of 34 total plots, is shown in Figure A-6. It has been redrawn from the original plot, however, for use in this report. Straight lines were then faired through the stress versus pressure plots from 0 to 5,000 psi,

and the resulting slopes or stress-pressure ratios, σ/p, were used to plot the points shown in Figures 7 and 8. The 0-to 5,000-psi pressure range was chosen because of the linear stress-pressure relationship in this region.

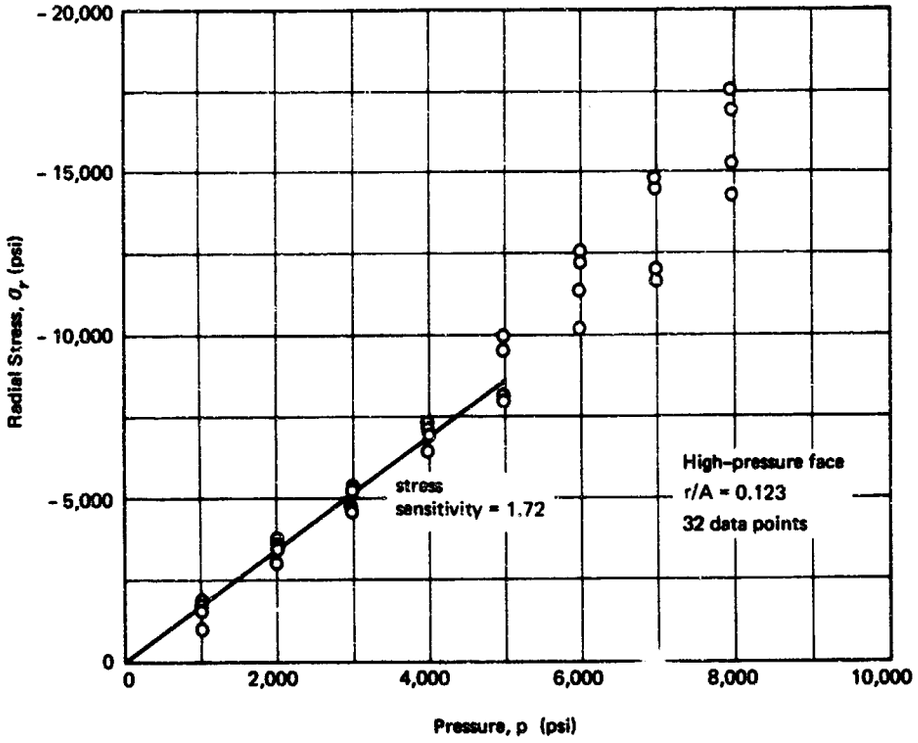

Figure A-6. Typical experimental stress versus pressure plot.

DISCUSSION

Two factors were present that required extra precautions in the strain gaging methods: (1) the viewports were made of plastic and (2) the gages would be exposed to a high-pressure environment. Mueller[9] performed experiments with strain gages mounted on acrylic plastic and proved that the heating of the substrate by the gage current can cause changes in the true strains. He also recommended the basic procedure that was followed in this report: a reduction in measuring current and short-time measurements at each recording station. Acrylic plastic has a low thermal conductivity and therefore cannot efficiently handle the gage heat load. This situation is compounded with the RTV compound placed on top of the gage as mechanical protection. Even with normal gage currents, large errors would result due to poor heat dissipation into plastic. The commonly used gage current of 25 milliamperes with 120-ohm gages was too high and, besides causing zero drift in the gages, it would heat up the acrylic plastic whose material properties are very sensitive to temperature changes.

The heat produced by a gage is

$$P = \frac{V^2}{R} \qquad \text{(A-7)}$$

where P = heat (watts)

V = excitation voltage (volts)

R = gage resistance (ohms)

By reducing the voltage and increasing the resistance of the gage, the heat can be reduced. Gages with 350 ohms were used, and the DATRAN excitation voltage caused a 6-milliampere gage current. This essentially reduced the heat load by a factor of six over 120-ohm gages with 25-milliampere currents. This lowered excitation voltage did not, however, affect the accuracy of the system because the DATRAN is a null-balance, as opposed to an unbalanced, system which functions independently of the magnitude of the voltage excitation.

Self-temperature-compensating gages for plastics are difficult, expensive, and lengthy in time to produce. Plastics vary so much in their coefficient of thermal expansion that it is not feasible to use a general self-temperature-compensating gage. Achievement of a special melt, equivalent to a certain plastic, many times requires a trial and error process at the factory. A temperature-compensation block was used in the circuit and an expansion coefficient of 13 ppm/^{o}F was used, the largest available. A three-wire system was impossible because of the limited number of high-pressure penetrations. The time required to reach equilibrium was quite important in regard to temperature compensation with a dummy gage. It must be assumed in this method of compensation that both the dummy and the active gage are at the same temperature. The various active gages are then alternately switched into the circuit while the dummy gage remains continuously in the circuit. This practice may lead to errors since the circuit temperature of the dummy gage and the active gage will vary. A large percentage of this error was eliminated by dynamically balancing so that the unit would be properly balanced when switching from channel to channel.

Many times the errors attributed to gages in a high-pressure environment result from improper mounting techniques. The substrate or viewport in this case was machined to a 32 rms finish and then polished so the surface was flat, smooth, and void of pits and scratches. Great care was

taken to prevent bubbles in the cement line and to make it as thin and uniform as possible. The rosette type chosen was flat, as opposed to stacked, to eliminate any possible errors due to the hydrostatic pressure.

Brace[10] determined in his research on strain gages under high pressure, that the gages experienced a positive, linear apparent strain of 3.8 μin./in. per 1,000 psi which was independent of the elastic properties of the substrate. He used foil, epoxy-backed gages, and an epoxy adhesive. The tests ranged from 0 to 145,000 psi and were run with a kerosene pressure medium. Milligan[11] performed similar research with foil, epoxy-backed gages, but with Eastman 910 adhesive. His tests yielded positive linear results of 3.7, 5.0, and 5.5 μin./in. per 1,000 psi. The tests ranged from 0 to 140,000 psi and were run with a PLEXOL 201 environment.

The lowest strain recorded in this study was -2,060 μin./in. at 8,000 psi. Using a value of 5.5 μin./in. per 1,000 psi, the maximum error due to the hydrostatic effect on the strain gages was only 2.1%.

The scatter in the data above 5,000 psi was caused by the viewport entering into the nonelastic range. This is also evidenced in the plot of the low-pressure face displacements in Figure A-3. The highest strain recorded with the gages was -21,400 μin./in. (-2.14% strain) or still within the 4% strain working limit of the constantan gages.

For this initial study, the tests were run quickly (500 psi/min) to record only the instantaneous or elastic strains and not the creep strains. Every precaution was taken to eliminate any possible creep effects. The gages were alternately connected from each side of the center point of the viewport into the DATRAN unit to negate possible creep effects during the recording period. For example in Figure A-1, pattern two, the order of the rosettes wired to the unit was 1, 5, 2, 6, 3, 7, 4, 8.

The two volumes of the full-scale viewports differed by a factor of eight. This provided an opportunity to investigate scaling effects using both axial displacements and stress distributions for comparison. Figures A-3 and A-6 represent displacements and stresses, respectively, for both the 4-inch and 8-inch minor diameter viewports. The low-pressure face displacements were equivalent after normalization and the stress data were completely intermixed indicating again that no scaling effects were present.

FINDINGS

1. The null-balance DATRAN unit, in conjunction with 350-ohm, foil, epoxy-backed strain gages and Eastman 910 adhesive provided a satisfactory method for recording strains in acrylic plastic in a high-pressure oil environment.

2. The viewports, with a volume ratio of eight, were linearly scalable as evidenced by both the stresses and the normalized displacements.

3. The viewports appeared to leave the linear elastic range at 5,000-psi pressure as evidenced by both the stresses and normalized displacements.

Appendix B

HIGH-PRESSURE EQUIPMENT AND PROCEDURE FOR EXPERIMENTAL PHASE

INTRODUCTION

High-pressure equipment and an orderly procedure were necessary to conduct safely and expertly hydrostatic pressure tests up to 8,000 psi on four acrylic plastic viewports instrumented with strain gages.

HIGH-PRESSURE EQUIPMENT

A schematic of the high-pressure equipment is shown in Figure B-1.

High-Pressure Pump

The high-pressure pump, shown in Figure B-2, was an air-driven double-acting piston pump rated for 20,000 psi. Tubing made of 1/4-inch-diameter 316 stainless steel and rated at 30,000 psi was used in the high-pressure system.

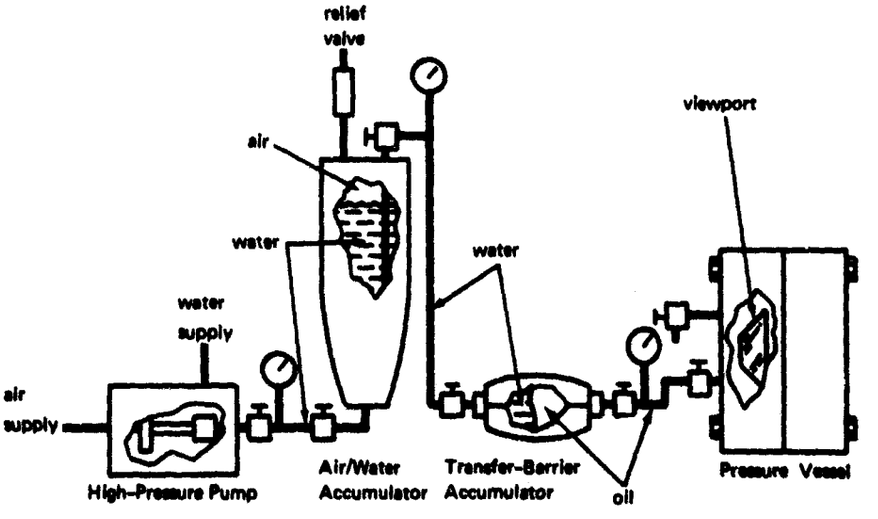

Figure B-1. Schematic of high-pressure equipment.

Figure B-2. High-pressure pump and pressure vessel.

Air/Water Accumulator

The air/water accumulator provided a means of storing energy in the high-pressure system to maintain a constant pressure in the pressure vessel. It also reduced the shock loads on the pressure gages by acting as a surge chamber and damping the cyclic shocks from the pump. The accumulator used was similar to the 16-inch, high-capacity naval projectile converted to a pressure vessel that is shown in Figure E-1 in Appendix E.

Transfer-Barrier Accumulator

A high-pressure transfer-barrier accumulator was necessary to separate the high-pressure water and the high-pressure oil in the system. The GREER 2-1/2-gallon accumulator used a flexible barrier between the oil and water.

Pressure Medium

A nonconducting oil was used in the pressure vessel to negate any shorting of the gages, if accidental leaks occurred in the waterproofing. The oil used was USP–XV mineral oil which was neutral to both the acrylic and the lead wire insulation.

Pressure Vessels

A typical pressure vessel for testing the acrylic viewports is shown in Figure B-2. The vessel consisted of two 32-inch-diameter flanges shown in Figure B-3. Two vessels were necessary for this experiment; one to hold the 8-inch minor diameter viewport and one for the 4-inch minor diameter viewport. The pertinent flange dimensions were as follows:

Nominal Flange Size (in.)	Included Angle, α	Through Hole Diameter (in.)
4	90^{o} 0' ± 5'	3.992
8	90^{o} 0' ± 5'	7.993

The flanges were designed to be rigid enough to preclude any additional loads on viewports due to flange deformation. The flanges were made of forged AISI 4140 steel and were bolted together with twelve 2-1/4-inch-diameter, 22-inch-long ASTM A193-B7 studs. The vessels used an O-ring face seal and had four small, equally spaced penetrations in each flange for the electrical penetrators. Both the mating surfaces of the flanges and the conical surface were machined to a 32 rms finish. The vessel, with the two flanges, could accommodate two viewports, but only one viewport was tested at a time. The other side was plugged with a universal cone that fit both vessels. The cone, with an 8-1/2-inch minor diameter, was made of 7075-T6 aluminum so it would not scratch the vessel surface; it utilized an O-ring in the conical face surface for sealing.

FULL-SCALE VIEWPORTS

The four full-scale viewports were rough cut from a 4-foot x 5-foot x 4-inch commercial sheet of Plexiglas G acrylic plastic. They were then rough-machined on a lathe before the first annealing. The annealing was performed to reduce or eliminate the internal stresses set

up during machining. The result was greater dimensional stability and greater resistance to crazing. Following is the manufacturer's recommended practice:[12]

Section Thickness (in.)	Oven Temperature (^{O}F)	Time (hr)	Cooling Rate (^{O}F/hr)
2	175	13	10
4	175	22	5

After the viewports cooled to 120^{O}F, they were removed from the annealing oven and cooled to room temperature. After machining to the dimensions shown in Table 1, they were polished to an optical finish and annealed again.

The maximum thickness of the viewports was limited to 4 inches because commercial grade acrylic sheets were available only to that thickness. It is possible, however, to laminate or custom cast thicker sections. Full-scale viewports as opposed to model viewports were used in the experimental stress analysis phase because they permitted more strain gages to be placed across the faces of the viewports and a more realistic simulation of the actual case.

Figure 8-3. Pressure vessel flanges.

TESTING PROCEDURE

Figure B-4 shows the experimental test setup just before a test. Prior to placing each viewport in the vessel, the conical face surfaces were coated with Dow Corning No. 4 silicone grease. The viewports were held in place with approximately 5-psi pressure while the high-pressure penetrator leads were connected to the DATRAN unit and the bridges balanced to zero. The whole system was allowed to reach room temperature equilibrium before the tests were started. The room temperature was maintained at 65 to 75°F throughout the tests.

The dial indicators were then mounted and zeroed. The pressure in the vessel was run up to 2,000 psi quickly and immediately dropped back to 5 psi. This was done to seat the viewport correctly in the flange and to squeeze out the excess grease. While at the 2,000-psi pressure, the dial indicators were checked for even deflection of the viewport. The strain gages and the dial indicators were then zeroed again before the test began. The tests were run by pressurizing the vessel at a rate of 500 psi/min with data recording at every 1,000-psi increment.

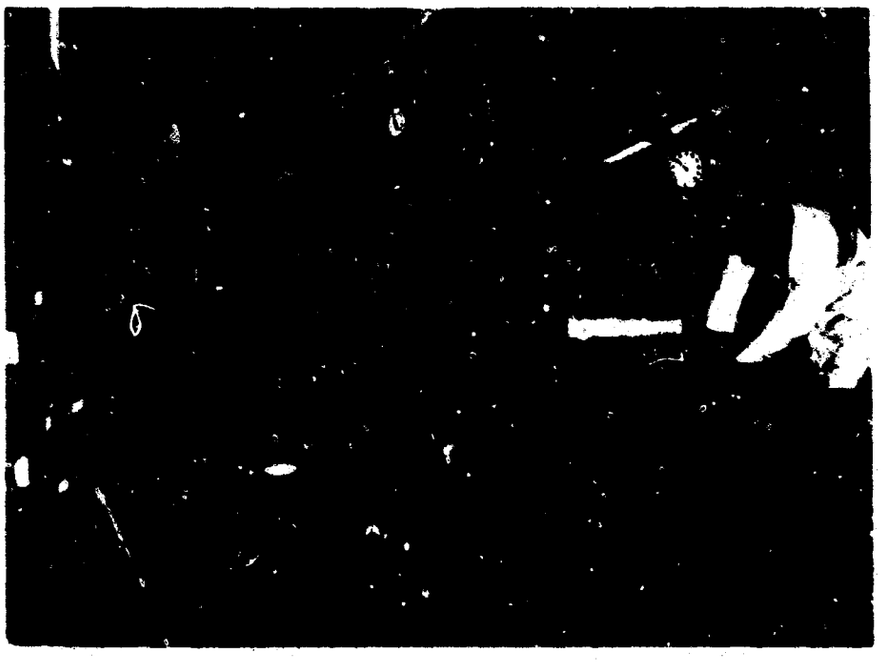

Figure B-4. Experimental test setup.

Appendix C

EXPERIMENTAL MEASUREMENT OF THE MODULUS OF ELASTICITY AND POISSON'S RATIO

INTRODUCTION

Values of the modulus of elasticity, E, and Poisson's ratio, ν, were used in the constitutive equations for both the finite element code and the reduction of the experimental data. The objective of this study was to determine experimentally the values of the two elastic constants, E and ν, because utilization of the handbook values could yield inaccurate results.

SCOPE OF INVESTIGATION

Four rectangular prisms with strain gages attached were tested. A typical specimen during test is shown in Figure C-1. Compressive values only for E and ν were deemed necessary because the majority of the stresses in the viewport were compressive. Because acrylic is extremely creep sensitive, care was taken to test all the specimens at the same rate. This rate was approximately the average loading rate of the experimental viewports. The temperature of the specimens during testing was maintained at 65 to 75^{o}F at all times.

TEST SPECIMENS

The rectangular prisms, which were easier to strain gage than cylinders, were cut from scrap left from the 4-foot x 5-foot x 4-inch sheets of acrylic out of which the viewports were cut. This was done to insure that the resulting E and ν were specifically applicable to the viewport data. The specimen sizes were 0.75 inch x 0.75 inch x 2.75 inches and they were all machined with plane and parallel faces. This size yielded a slenderness ratio of 12.7 which is between the limits of 11 and 15 prescribed by ASTM D 695-63T for plastic specimens, when the modulus of elasticity is desired. The standard specimen for compressive strength only is in the form of a right cylinder or prism whose length is twice its principal width or diameter.

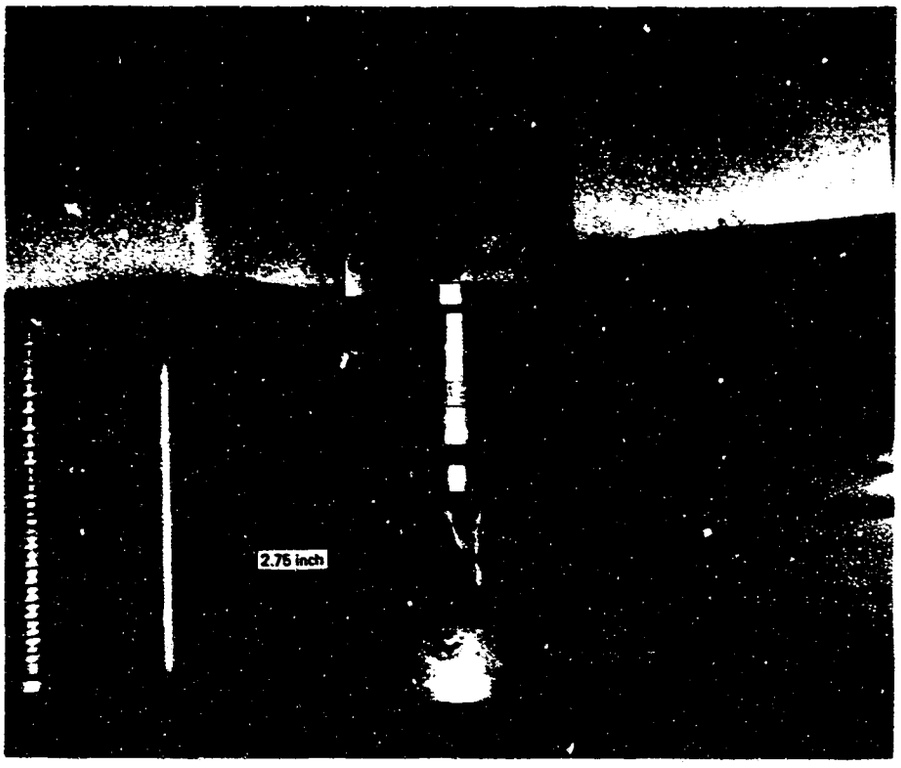

Figure C-1. Typical material properties specimen.

STRAIN GAGE INSTRUMENTATION

Baldwin-Lima-Hamilton FAET-12A-35S13WL strain gages were used. The same procedure that was used for mounting the gages on the viewports was followed for the compression specimens.

Two rosettes were mounted on each specimen, with the second rosette mounted on the face opposite the first. A half-bridge circuit was used with a dummy temperature-compensation block located nearby. The same Budd DATRAN digital strain indicator that was used with the viewports was also used in these tests. The two-gage, 90°, rectangular rosettes, which were necessary to pick up the Poisson strain, were mounted in the center of the specimens in accordance with Saint-Venant's principle on end effects.

COMPRESSION TESTING EQUIPMENT

A Tinius Olsen, 30,000-pound testing machine provided the means for testing the acryiic specimens. The specimens were tested to 7,500 pounds at a rate of 600 lb/min at which point the test was discontinued. Strains were recorded for every 500 pounds of load. Care was taken to select this correct pacer speed to insure a constant stressing rate of 1,070 psi/min.

REDUCTION OF DATA

The digital readout of the DATRAN unit was for gages in a biaxial strain field and, therefore, yielded only apparent strains. The same method and equations described in Appendix A were used to find the true strains. The same strain gage circuitry and mounting techniques used with the viewports were purposely used here to negate the addition of any new variables.

The true axial strains, as opposed to Poisson strains, from the eight axial gages were then plotted along with the stresses to yield an engineering stress-strain diagram. From this diagram, shown in Figure C-2, the modulus of elasticity in the linear region was found to be 444,000 psi.

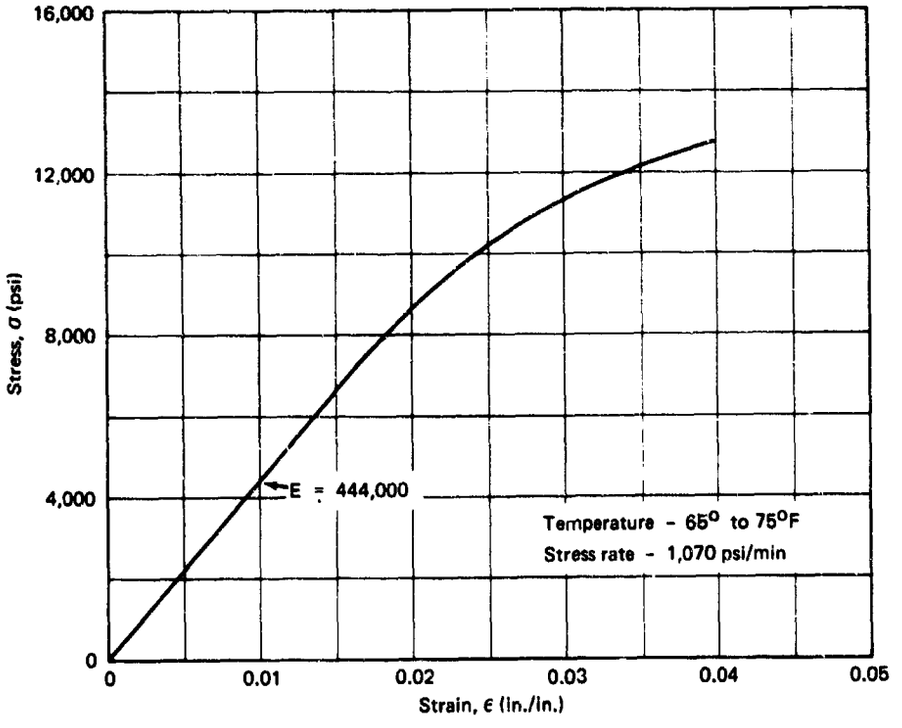

Figure C-2. Compressive stress-strain diagram for acrylic plastic.

The true Poisson strains from the eight Poisson gages were plotted against the stresses and a curve was faired through the points. The modulus of elasticity and the slope of the Poisson strain-stress curve over the same stress range were used to find ν.

Poisson's ratio, ν, is defined for uniaxial loading as follows

$$\nu = \frac{-\epsilon_{Poisson}}{\epsilon_{axial}} \qquad \text{(C-1)}$$

Dividing by the incremental stress change, $\Delta\sigma$

$$\nu = - \left(\frac{\Delta\epsilon_p}{\Delta\sigma}\right)\left(\frac{\Delta\sigma}{\Delta\epsilon_a}\right) \qquad \text{(C-2)}$$

but

$$\frac{\Delta\sigma}{\Delta\epsilon_a} = E$$

so

$$\nu = -E \left(\frac{\Delta\epsilon_p}{\Delta\sigma}\right) \qquad \text{(C-3)}$$

where $\Delta\epsilon_p/\Delta\sigma$ is the slope of the Poisson strain-stress curve. Using Equation C-3 and the previously found value of 444,000 psi for **E**, ν was found to equal 0.4.

DISCUSSION

Acrylic plastic mechanical properties are extremely temperature sensitive and, therefore, it is important that the temperature be controlled during any structural tests. As with all thermoplastics, total deformation increases with an increase in temperature. Therefore, tests run at room temperature will yield conservative results when compared to the viewport in actual service in the colder ocean.

Acrylic plastic is strain-rate sensitive as are many metals.[13,14] There are three types of deformations in amorphous polymers: (1) elastic, which is instantaneous and completely recoverable; (2) plastic, which leads to irrecoverable deformation; and (3) time-dependent deformation, which may or may not lead to permanent set. Tests that are run quickly should pick up only instantaneous stresses, thus minimizing creep. This investigation concerned itself only with the linear elastic stresses. The **E** and ν values are compared below to the handbook values.

Property	Handbook[12]	Experimental
Modulus of elasticity, E	450,000	444,000
Poisson's ratio, ν	0.35	0.4

The engineering stress-strain curves extend only to 4% strain because the gages used were not post-yield and therefore their accuracy is questionable above 4%. The strain data for all the specimens was very consistent,indicating no bending in specimens during testing due to eccentric loading.

Another test was run on sample coupons taken from the viewport scraps. This test was one of pure hydrostatic loading on a coupon with strain gages attached to determine the bulk modulus for acrylic plastic. The results of four coupons with a rosette apiece or eight gages are shown in Figure C-3. The strain gages, mounting procedure, and instrumentation were exactly the same as for the compression specimens. The pressurization rate was 1,000 psi/min.

The theoretical strain on a coupon under hydrostatic loading is derived as follows

$$\epsilon_r = \frac{1}{E} [\sigma_r - \nu (\sigma_\theta + \sigma_z)] \qquad \text{(C-4)}$$

where ϵ_r = radial true normal strain (in./in.)

E = modulus of elasticity (psi)

ν = Poisson's ratio

$\sigma_r, \sigma_\theta, \sigma_z$ = radial, tangential, and axial normal stresses (psi)

The three principal stresses are all equal to the pressure, -p, so

$$\epsilon = \frac{-p}{E} (1 - 2\nu) \qquad \text{(C-5)}$$

Substituting the previously found values of E and ν into Equation C-5, the resulting curve is shown in Figure C-3 along with the experimentally measured strain. The difference in the two curves at 8,000 psi is 280 μin./in. or 7.8%. Using a value of 5.5 μin./in. per 1,000 psi for the hydrostatic effect on the gages, the difference increased to 324 μin./in. or 9.0%. Actually the 9% difference is much better than it first appears. This is a severe test of elastic properties, as Equation C-5 is very sensitive to a change in Poisson's

ratio. The 9% difference in strains can be erased with a 2.5% decrease in ν or a change in ν from 0.4 to 0.39. The values for E and ν thus appear to correlate with the compressive specimen results.

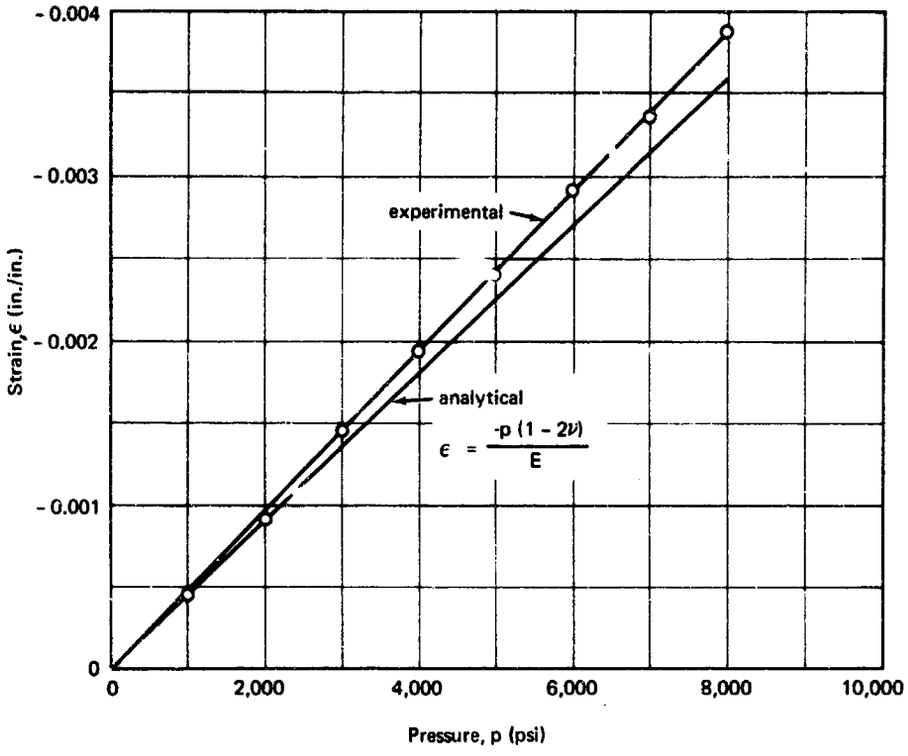

Figure C-3. Hydrostatic verification of material properties.

The bulk modulus is defined as follows

$$K' = \frac{-p}{J_1} \qquad \text{(C-6)}$$

where K' = bulk modulus of elasticity (psi)

p = pressure (psi)

J_1 = first invariant of strain (in./in.)

From Equation C-6, the bulk modulus was found to equal 740,000 psi.

FINDINGS

Plexiglas G acrylic plastic exhibited the following compressive properties for a stress rate of 1,070 psi/min and a temperature of 65 to 75°F.

1. The modulus of elasticity was found to equal 444,000 psi while Poisson's ratio was found to equal 0.4.

2. The bulk modulus of elasticity was found to equal 740,000 psi.

3. The linear elastic range was assumed to end at 0.017 in./in. and 7,500 psi.

Appendix D

FINITE ELEMENT METHOD USED IN ANALYTICAL PHASE

INTRODUCTION

The second objective of this study was to perform an analytical analysis of the viewport using a relatively new technique called the finite element method. Although this unique method is analytical, it exhibits many of the advantages of a direct experimental procedure in that it can handle complex shapes and boundary conditions.

The theory of elasticity provides classical solutions for states of stress/strain in solid bodies under load. The theory provides a complete solution for cases where the bodies have simple shapes and are subjected to simple boundary conditions. When using the theory of elasticity, the body must be completely described mathematically. These mathematical equations, however, often cannot be written for the complex loads and shapes that are actually encountered. Even if the equations are written, they may be extremely difficult to solve. Therefore, in actual engineering problems where either the shape of the body or the boundary conditions are not simple, the theory provides at most an approximate solution.

It is for this reason that experimental stress analysis methods were devised. These methods include such techniques as photoelastic model studies and coatings, strain gages, and brittle coatings. In the past, experimental stress analysis techniques have provided the only solutions to complex problems which could not be solved analytically.

The finite element method[15] bypasses the mathematical descriptions yet maintains the advantage of giving accurate results throughout the body. In fact, the finite element results for homogeneous, isotropic, linearly elastic solids converge to known exact or closed-form classical solutions as the number of elements is increased.

The conical viewport problem has no known closed-form solution, since the skew boundary and plugging effect make the mathematical description difficult. A solution to the viewport problem was accomplished, however, by a finite element analysis. The solution is compared to both photoelastic and strain gage results in the main text in Figures 7 and 8.

FINITE ELEMENT COMPUTER PROGRAM

The finite element computer program used in this study is a general program for solids-of-revolution with an axisymmetric load. The code, which was written by Wilson,[16] may be used to analyze the linear elastic response of an axisymmetric solid consisting of an isotropic, homogeneous material. The basic program, exclusive of the mesh-generator and plotter routines, is listed in a report by Takahashi and Dong.[17]

The analysis in this study began with an idealization of the viewport with a finite number of elements connected at a finite number of nodal points. The mesh, along with the number of elements and nodal points, is shown in Figure D-1. The program accepts either quadrilateral (four constant strain triangles) or triangular elements. A mesh-generator routine reduced the time involved in breaking the viewport down into individual elements.

Because the three-dimensional viewport is axisymmetrical, the analysis reduced to a two-dimensional plane strain problem with 2 degrees of displacement freedom at each node (axial and radial) which are prescribed either fixed or free. The loading is arbitrary and may be applied either as a static pressure or a concentrated load. The input to the code consisted of the number of node points in the mesh idealization (900 max), number of elements (800 max), the geometry of the mesh, the physical properties of the acrylic plastic (Appendix C), and the stress and displacement boundary conditions. The output consisted of the input data, displacements of each node point, stresses at the centroid of each element, and the various contour plots.

The entire code was written in Fortran IV and required four tapes and 65,000 words of core storage. The plot routines used standard SC 4020 software.[8] Using overlay, the program was run on an IBM 7094 II typically requiring 9 minutes per problem. A data tape is created by the computer to drive the plotter. The SC 4020 plotter uses a standard 35mm motion picture camera to record the images drawn on the cathode ray tube by the plot routines. The stress and displacement contours, displaced shape, and mesh idealization shown in this report were drawn by the plotter.

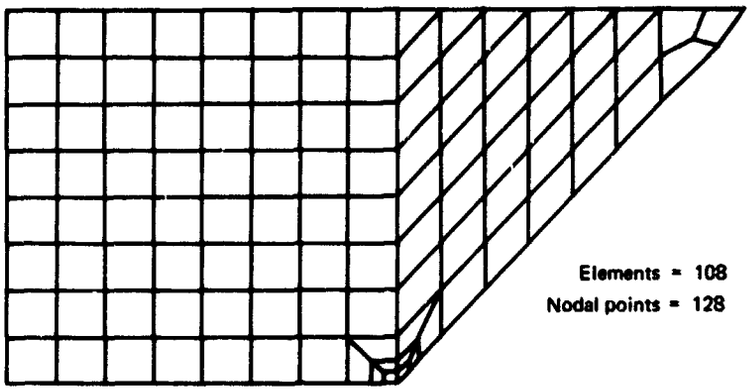

(a) Coarse mesh.

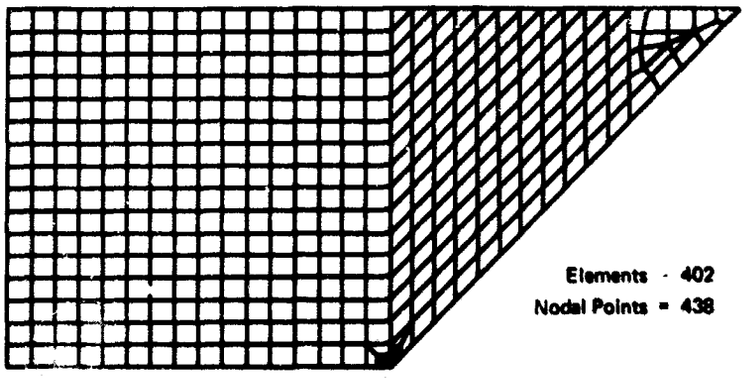

(b) Fine mesh.

Figure D-1. Finite element mesh for viewport analysis.

DISCUSSION

The exact friction factor along the viewport edge was unknown so two types of boundary conditions, fixed and free, were employed to bracket the actual case. Fine and coarse meshes, as shown in Figure D-1, were used to check convergence for each type of boundary condition. Convergence is demonstrated in Figure D-2 by comparing the axial displacements along the low-pressure face for both the fine and coarse meshes.

Due to the skew boundary and nonorthogonal corners, the analytical behavior of the viewports is mesh sensitive, and care and experience must be used in drawing the mesh. Although some local improvements to the results could be obtained by further refinements to the mesh, only a slight global improvement would occur. Special attention was given to drawing the mesh in the two corners of the viewport to isolate the effects of the stress concentration at the low-pressure corner and to allow the free flow of stresses through the corner of the high-pressure face.

FINDINGS

1. The addition of plotter and mesh-generator routines to a finite element computer program greatly enhances the program's usefulness.

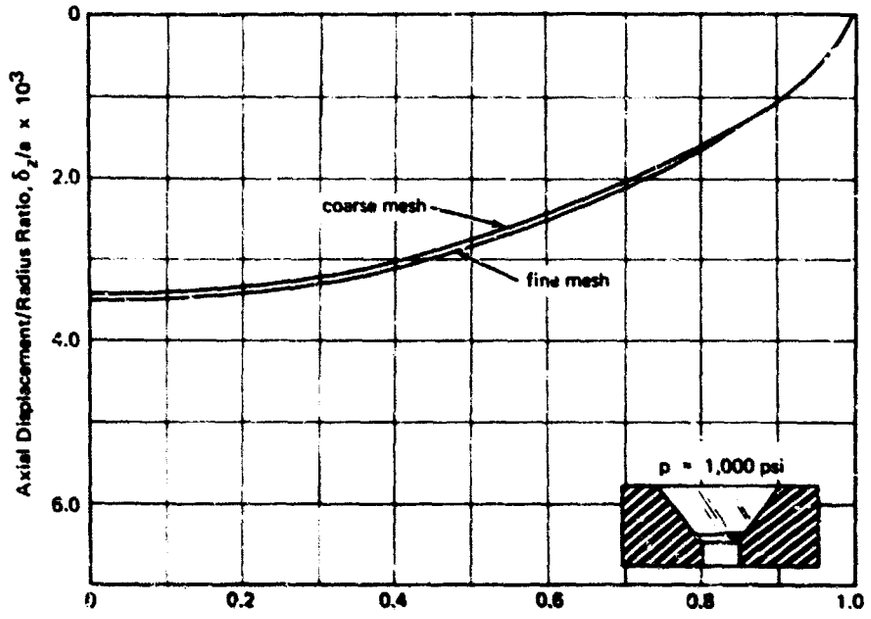

(a) Fixed boundary.

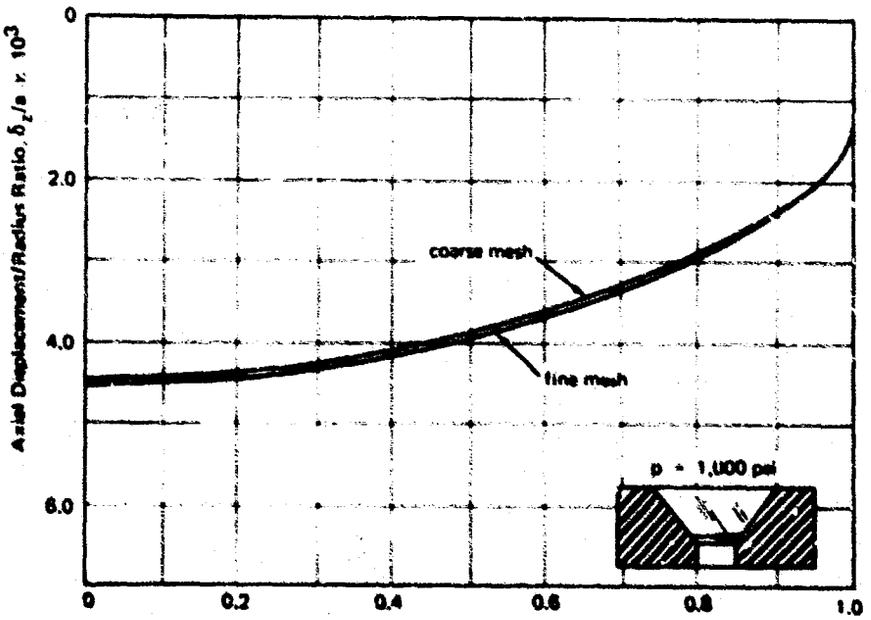

(b) Free boundary.

Figure D-2. Comparison of fine and coarse mesh displacements across low pressure face.

Appendix E

FLANGE SURFACE FINISH EFFECTS ON MODEL VIEWPORTS

INTRODUCTION

The third objective of this study was to determine the effect, if any, of the flange surface finish on the structural behavior of the viewport. This appendix presents detailed information on the model viewports, the method of testing, and the post-test visual observations.

MODEL VIEWPORTS

The 15 viewports were all machined from the same 1-inch-thick sheet of "G" grade unshrunk Plexiglas to insure equal mechanical properties. The viewports were first machined to a 32 rms finish and then all faces were polished to an optical finish, which would allow easier visual inspection of viewport cracks. The viewport dimensions are given in Table E-1.

HIGH-PRESSURE EQUIPMENT

A 16-inch Naval gun shell converted to a pressure vessel[18] capable of static pressures in excess of 20,000 psi was used and is shown in Figure E-1. The pressurizing medium was tap water maintained at 65 to 75°F. The flange, shown in Figure E-2, was fabricated out of mild steel and had the following measured pertinent dimensions:

Flange Surface Finish (rms)	Included Angle, α	Through Hole Diameter (in.)
32	90° 30′ ± 5′	1.002
63	90° 20′ ± 5′	1.002
125	90° 30′ ± 5′	0.998

Utilizing a three-viewport flange such as this enabled all parameters to be held constant except for the surface finish. The root-mean-square (rms) roughness is defined as the average of the height deviations measured in microinches between the mean and actual surfaces.

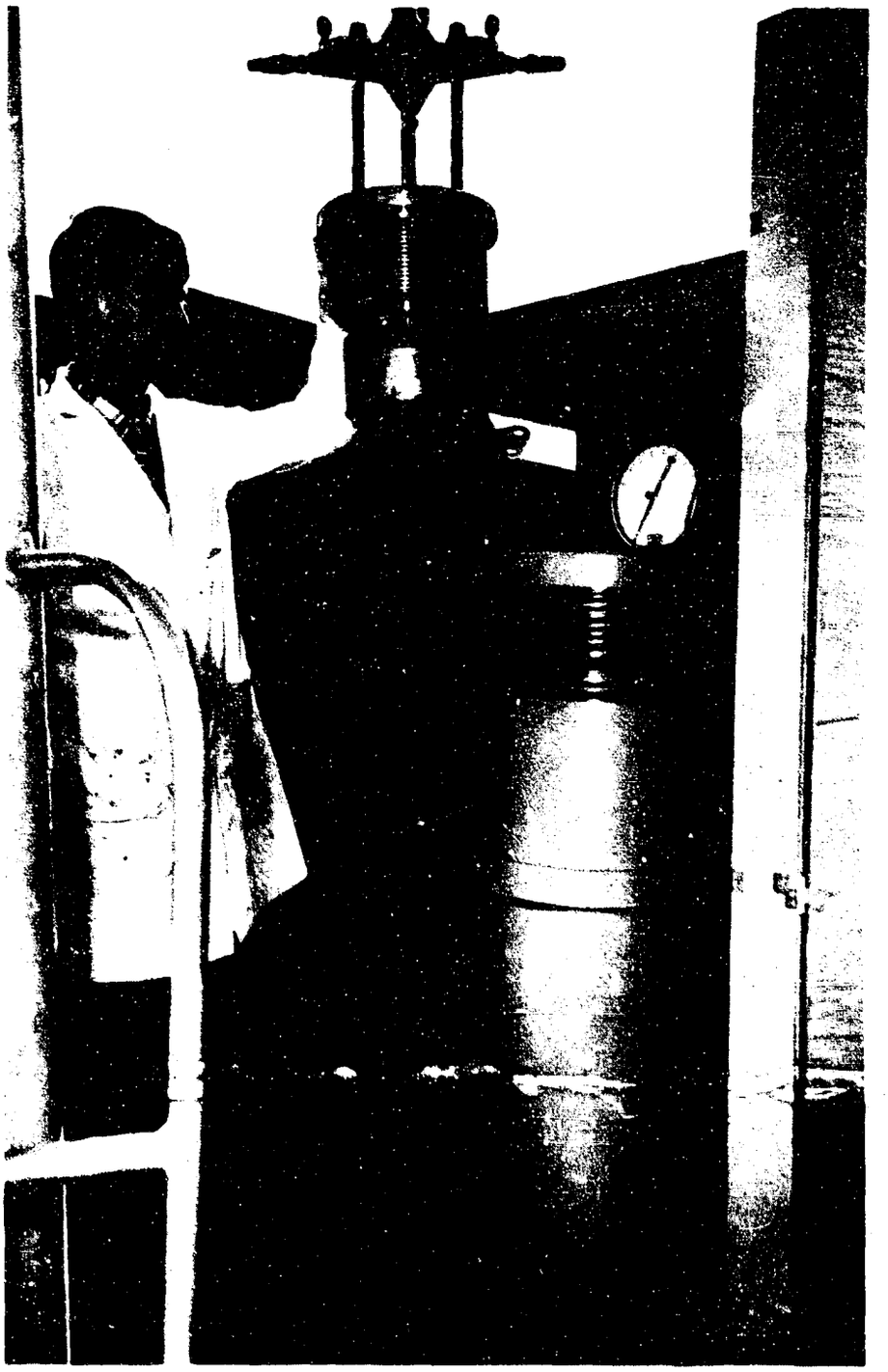

Figure E-1. Pressure vessel converted from 16-inch Naval gun shell.

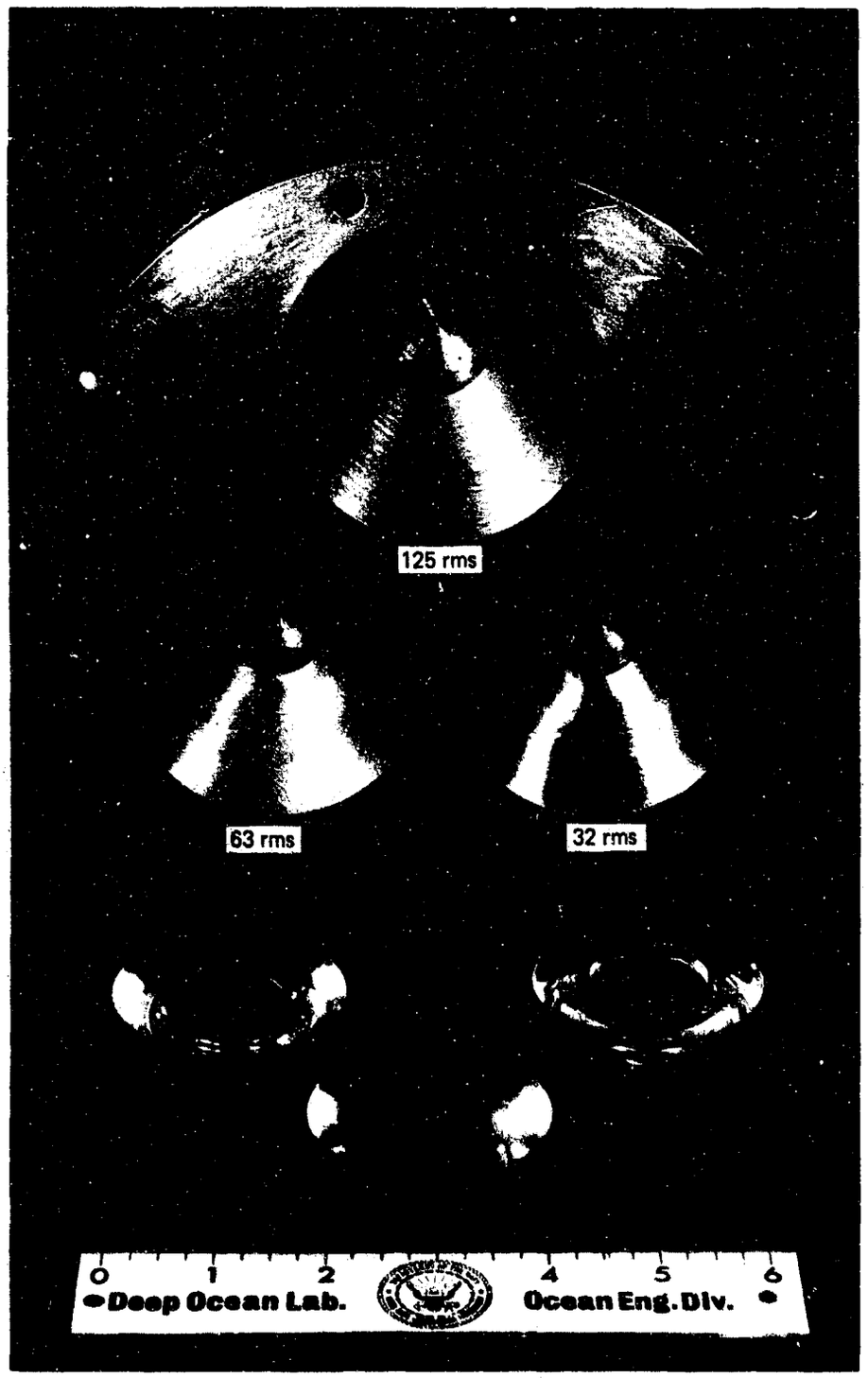

Figure E-2. Flange for surface finish tests.

Table E-1. Model Viewport Dimensions

Included Angle, α^a	Major Diameter, D (in.)	Minor Diameter, d (in.)	Thickness, t (in.)	t/d
90° 10′	2.307	1.058	0.623	0.589
90° 20′	2.309	1.058	0.622	0.588
90° 0′	2.310	1.060	0.625	0.590
90° 10′	2.307	1.054	0.625	0.593
90° 30′	2.310	1.055	0.622	0.590
90° 10′	2.308	1.061	0.622	0.586
90° 0′	2.310	1.062	0.624	0.588
90° 20′	2.309	1.058	0.622	0.588
90° 20′	2.309	1.052	0.625	0.594
90° 10′	2.310	1.057	0.625	0.591
90° 20′	2.308	1.055	0.623	0.590
90° 0′	2.310	1.060	0.625	0.590
90° 30′	2.310	1.055	0.622	0.590
90° 10′	2.306	1.053	0.625	0.594
90° 30′	2.310	1.054	0.623	0.591

[a] Included angle ± 5 minutes.

TEST PROCEDURE

After all model viewports were measured and the data recorded, three viewports at a time were arbitrarily chosen to assure randomness in angle and diameter mismatch A thin layer of silicone lubricant, Dow Corning No. 4, was applied to the conical surfaces to hold the viewports in place and for initial sealing. A plate of shim stock was bolted over the flange seats to prevent the viewports from falling into the pressure vessel upon

completion of the test. Each set of three viewports was then pressurized at 1,000 ± 50 psi/min to 23,000 psi, at which point the pressure was bled off immediately and the cycle repeated. This procedure was repeated five times. The new physical dimensions were measured and recorded in Table 3.

POST-TEST VISUAL OBSERVATIONS

Figure 12 shows typical cross sections of the model viewports after testing, whereas this section describes in more detail the post-test visual observations.

Viewports in Flange with 125 RMS Surface Finish

High-Pressure Face. All five of the viewports had slight, but visible concave depressions centrally located on this face. These craters averaged 1/2 inch in diameter and had minimal stress crazing at the periphery.

Conical Surface. All five of the viewports had grip marks beginning at the low-pressure face end and extending halfway up the conical surface. The grip marks were a result of embossing from the 125 rms flange finish and can be seen in Figure E-3. There were numerous crazing cracks on this face 0.1 inch above the low-pressure face. The cracks were infinitesimally small, completely separate from one another, and were only discernible when held in a particular position with respect to the eye and the light source.

Low-Pressure Face. All five of the viewports exhibited permanent extrusion on this face. The permanent set was not uniform across the face, however, in that it consisted of a ridge approximately 0.05-inch wide around the circumference of the face. It is the height of this ridge that is listed as the permanent extrusion in Table 3.

Viewports in Flange with 63 RMS Surface Finish

High-Pressure Face. Three of the viewports in this group had a semicircular crack extending from the conical surface through to the high-pressure face, as shown in Figure E-4. The crack broke the surface where the crazing cracks were located around the crater; the viewports, however, remained intact. The remaining two viewports in this group exhibited only an increase in crater depth over that of the 125 rms viewports. It was noticed that there were perpendicular cracks propagating from the high-pressure face which originated at the crater periphery.

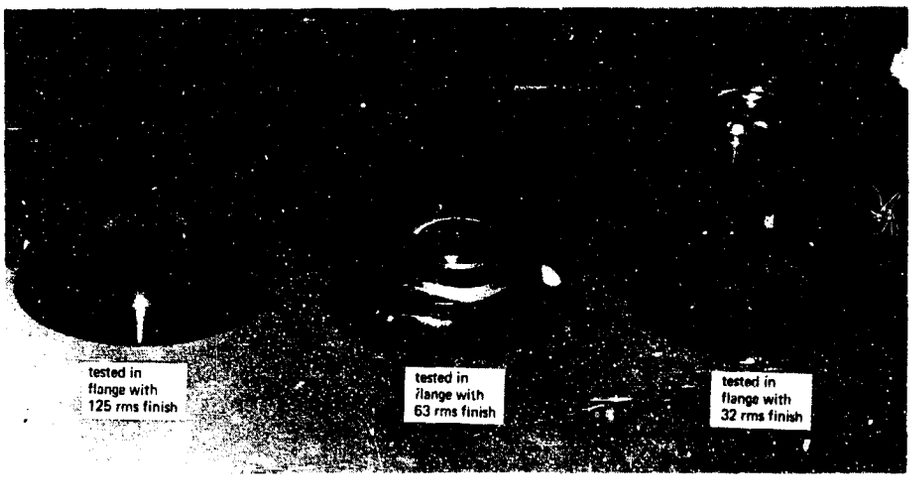

Figure E-3. Model viewports after test, set 1.

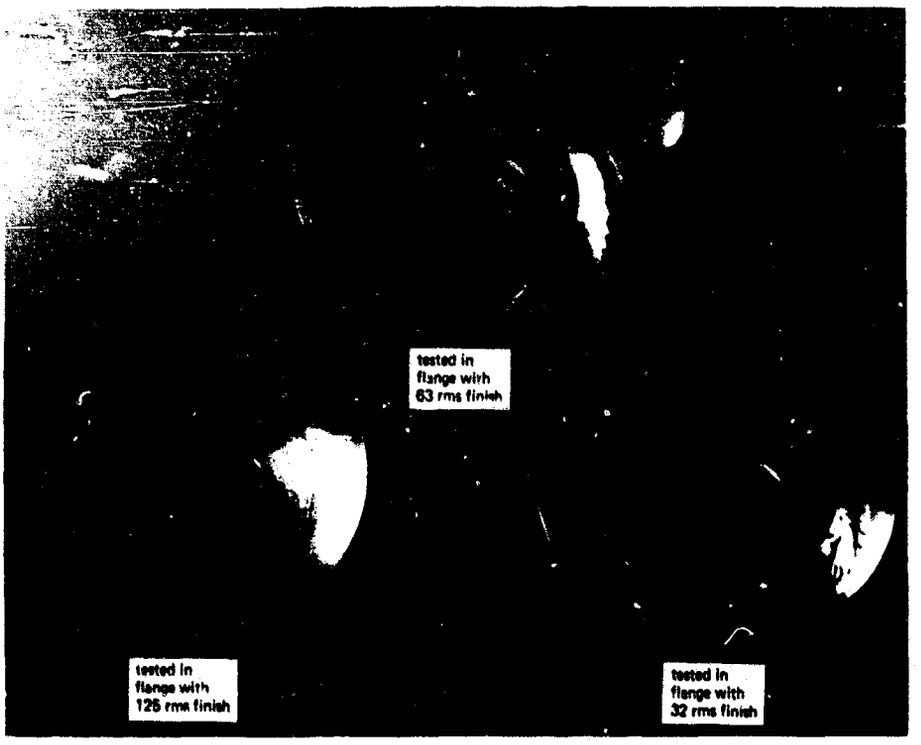

Figure E-4. Model viewports after test, set 3.

Conical Surface. All five viewports exhibited infrequent and barely discernible grip marks evenly distributed on this face. Two viewports had cracks extending halfway to the high-pressure face beginning 0.1 inch above the low-pressure face. The cracks initiated perpendicular to the conical surface, but tended to bend upward to the high-pressure face crater perimeter. The three remaining viewports had the same types of cracks extending completely to the high-pressure face.

Low-Pressure Face. All five viewports were void of any cracks on this face. The extrusion increased over that of the viewports in the 125 rms flange. The permanent extrusion is clearly shown in Figure E-3.

Viewports in Flange with 32 RMS Surface Finish

High-Pressure Face. Two of the viewports in this group separated into two pieces as shown in Figure E-3. The high-pressure face exhibited two concentric circles of cracks. The smaller diameter crack originated from the perimeter of the crater, whereas the larger diameter crack was the one that separated the two pieces. It was noticed that the cracks always were perpendicular to the broken surfaces. Two of the remaining three viewports had a complete circular crack located at the perimeter of the crater as shown in Figure E-4. The fifth viewport in this group had only a semicircular crack.

Conical Surface. The two separated viewports had two major cracks on the conical surface along with the stress crazing. One crack was the separation crack, while the other initiated 0.1 inch above the low-pressure face and propagated at some locations as far as the high-pressure face. This face did have grip marks although they were less in number than in the 63 rms viewports. The three remaining viewports had only one large crack located among the stress crazing cracks.

Low-Pressure Face. All five viewports were void of cracks located on this face and still maintained a ridge around the low-pressure face with the ridge heights as noted in Table 3.

REFERENCES

1. M.R. Snoey and J.D. Stachiw. "Windows and transparent hulls for man in hydrospace," in A critical look at marine technology; transactions of the 4th annual MTS conference & exhibit, Washington, D.C., July, 8-10, 1968. Washington, D.C., Marine Technology Society, 1968, pp. 419-463.

2. A. Piccard. Earth, sky and sea. New York, Oxford University Press, 1956.

3. Allied Research Associates, Inc. Technical Report ARA 315-7: A photoelastic investigation of deep submergence windows, by R. Winter and H. Becker. Concord, Mass., May 1966. (Contract NObs-94102) (AD 634403).

4. Allied Research Associates, Inc. Technical Report ARA 315-10: An experimental investigation of deep submergence windows, by R. Winter. Concord, Mass., Oct. 1966. (Contract NObs-94102) (AD 640707).

5. Armed Forces Supply Support Center. Military Handbook MIL-HDBK-17: Plastics for flight vehicles, pt, 2. Transparent glazing materials. Washington, D.C., Aug. 1961.

6. C.C. Perry and H.R. Lissner. The strain gage primer, 2d ed. New York, McGraw-Hill, 1962, pp. 157-163.

7. S. Timoshenko and J.N. Goodier. Theory of elasticity, 2d ed. New York, McGraw-Hill, 1951.

8. Pacific Missile Range. Test Data Division. Technical Note No. 3285-2-65: Modifications of North American's engineer's computing manual for General Dynamics' SC-4020 plotter in use at PMR, by D.M. Profant. Point Mugu, Calif., August 1965. (Originally published as: North American Aviation, Inc. Engineering computing manual, Oct. 1963.)

9. R.K. Mueller. "The influence of measuring current and preheating on measurements on resins with electric-resistance strain gages," Experimental Mechanics, vol. 5, no. 11, Nov. 1965, pp. 19A-26A.

10. W.F. Brace. "Effect of pressure on electric-resistance strain gages," Experimental Mechanics, vol. 4, no. 7, July 1964, pp. 212-216.

11. R.V. Milligan. "The effects of high pressure on foil strain gages," Experimental Mechanics, vol. 4, no. 2, Feb. 1964, pp. 25-36.

12. Rohm and Haas Company. Publication no. PL-28n: PLEXIGLAS design and fabrication data, Rev. ed. Philadelphia, Pa., Sept. 1964.

13. C.J. Maiden and S.J. Green, "Compressive strain-rate tests on six selected materials at strain rates from 10^{-3} to 10^{4} in./in./sec," Journal of Applied Mechanics, vol. 33, no. 3, Sept. 1966, pp. 496-504.

14. J.D. Chaluprnik and M.R. Snoey. "Dynamic deformations in metals," in Proceedings, 7th International Symposium on Space Technology and Science, Tokyo, May 1967, edited by Y. Kuroda. Tokyo, Japan, Maruzen Co., 1968, pp. 219-227.

15. O.C. Zienkiewicz. The finite element method in structural and continuum mechanics. New York, McGraw-Hill, 1967.

16. E.L. Wilson. "Structural analysis of axisymmetric solids," American Institute of Aeronautics and Astronautics, Journal, vol. 3, no. 12, Dec. 1965, pp. 2269-2274.

17. Naval Civil Engineering Laboratory. Technical Report R-567: Finite element analyses of solids of revolution, by S.K. Takahashi and S.B. Dong. Port Hueneme, Calif., Mar. 1968. (AD 667235).

18. Naval Civil Engineering Laboratory. Technical Note N-755: The conversion of 16-inch projectiles to pressure vessels, by K.O. Gray and J.D. Stachiw. Port Hueneme, Calif., June 1965. (AD 625950).

LIST OF SYMBOLS

A	Radius of high-pressure face, in.
a	Radius of low-pressure face, in.
D	Diameter of high-pressure face, in.
d	Diameter of low-pressure face, in.
E	Modulus of elasticity, psi
h	Elevation of viewport in flange, in.
J_1	First invariant of strain, in./in.
K	Transverse sensitivity of strain gage
K'	Bulk modulus of elasticity, psi
P	Heat, watts
p	Pressure applied to viewport, psi
R	Resistance of strain gage, ohms
r	Radial coordinate, in.
t	Thickness of viewport, in.
V	Excitation voltage, volts
z	Axial coordinate, in.
α	Included angle of conical viewport, deg
δ_r, δ_z	Radial and axial displacements of viewports, in.
$\epsilon_r, \epsilon_\theta, \epsilon_z$	Radial, tangential, and axial true normal strains, in./in.
$\epsilon'_r, \epsilon'_\theta, \epsilon'_z$	Radial, tangential, and axial apparent normal strains, in./in.
θ	Tangential coordinate, deg
ν	Poisson's ratio
$\sigma_r, \sigma_\theta, \sigma_z$	Radial, tangential, and axial normal stresses, psi

Unclassified
Security Classification

DOCUMENT CONTROL DATA - R & D

Security classification of title, body of abstract and indexing annotation must be entered when the overall report is classified)

1. ORIGINATING ACTIVITY (Corporate author)	2a. REPORT SECURITY CLASSIFICATION
Naval Civil Engineering Laboratory Port Hueneme, California 93041	Unclassified
	2b. GROUP

3. REPORT TITLE

STRESS ANALYSIS OF A CONICAL ACRYLIC VIEWPORT

4. DESCRIPTIVE NOTES *(Type of report and inclusive dates)*

Final; April 1967–April 1969

5. AUTHOR(S) *(First name, middle initial, last name)*

M. R. Snoey and J. E. Crawford

6. REPORT DATE	7a. TOTAL NO. OF PAGES	7b. NO. OF REFS
April 1970	65	18

8a. CONTRACT OR GRANT NO.	9a. ORIGINATOR'S REPORT NUMBER(S)
b. PROJECT NO. YF 38.535.005.01.005	TR-675
c.	9b. OTHER REPORT NO(S) *(Any other numbers that may be assigned this report)*
d.	

10. DISTRIBUTION STATEMENT

This document has been approved for public release and sale; its distribution is unlimited.

11. SUPPLEMENTARY NOTES	12. SPONSORING MILITARY ACTIVITY
	Naval Facilities Engineering Command Washington, D. C.

13. ABSTRACT

This study was initiated to: (1) determine experimentally the structural response of a viewport design, (2) determine the accuracy of the finite element method in predicting viewport behavior by comparing analytical to experimental results, and (3) determine the effect, if any, of the flange surface finish on the structural behavior of the viewport using both experimental and analytical techniques. In the experimental phase, four, full-scale, conical acrylic viewports, with a nominal thickness-to-minor-diameter ratio of 0.5 and an included angle of 90^{0}, were strain-gaged and tested to 8,000 psi. In the analytical phase, the same viewport design was analyzed with a finite element computer program. The finite element results successfully bracketed the experimental results by assuming two extreme boundary conditions, fixed and free, at the viewport-flange interface. The fixed condition assumed an infinite coefficient of friction, and the free condition assumed zero friction. In addition, the finite element analysis provided complete internal stress distributions. All results indicated that viewports with this design exhibit both plugging and bending behavior and have two areas of high stress concentration, the center of the high-pressure face and the corner between the low-pressure face and the conical bearing surface. The analytical investigation indicated that the surface finish of the flange significantly affects the viewport stress distribution.

DD FORM 1 NOV 65 1473 (PAGE 1)

S/N 0101-807-6801

Unclassified
Security Classification

14 KEY WORDS	LINK A		LINK B		LINK C	
	ROLE	WT	ROLE	WT	ROLE	WT
Acrylic plastic						
Plexiglas						
Undersea vehicles						
Habitats						
Submersibles						
Finite element						
Deep submergence						
Stress analysis						
Windows						
Hydrostatic pressure tests						
Pressure vessels						
Conical viewports						